

Physics-informed post-processing of stabilized finite element solutions for transient convection-dominated problems

Süleyman Cengizci^{a,*}, Ömür Uğur^b, Srinivasan Natesan^c

^a*Department of Computer Technologies, Antalya Bilim University, Antalya 07190, Turkey*

^b*Institute of Applied Mathematics, Middle East Technical University, Ankara 06800, Turkey*

^c*Department of Mathematics, Indian Institute of Technology Guwahati, Guwahati 781039, India*

Abstract

The numerical simulation of convection-dominated transient transport phenomena involves significant computational challenges due to the presence of sharp gradients and propagating fronts across the spatiotemporal domain. Classical numerical discretization methods often produce spurious oscillations, necessitating advanced stabilization strategies. Moreover, even when stabilization suppresses such numerical instabilities, additional regularization may still be required to resolve localized sharp gradients. Conversely, standalone physics-informed neural network (PINN) methods struggle to capture sharp layers arising in convection-dominated problems and typically require a prohibitively large number of training epochs to learn the solution from scratch. To this end, this work presents a hybrid computational framework—extending the PASSC (PINN-Augmented SUPG with Shock-Capturing) methodology, originally developed for steady problems, to the unsteady regime—that combines stabilized finite element methods (FEM) with PINNs for solving transient convection-diffusion-reaction (CDR) equations. A semi-discrete stabilized finite element method is adopted, where stabilization is achieved through the streamline-upwind/Petrov–Galerkin (SUPG) formulation augmented with a $YZ\beta$ shock-capturing operator to resolve steep gradients and shock-like features. Rather than training over the entire spatiotemporal domain, a PINN-based post-processing correction is applied selectively near the terminal time, where the neural network enhances the finite element solution by assimilating spatial data from the last K_s snapshots while enforcing residual constraints derived from the governing equations and boundary conditions. The network architecture employs residual blocks with random Fourier features to efficiently capture multiscale solution structures, and a progressive training strategy with adaptive loss weighting balances data fidelity and physical consistency. Comprehensive numerical experiments on five benchmark problems—including boundary and interior layers, traveling waves, and nonlinear Burgers dynamics—demonstrate that the proposed framework markedly improves solution accuracy at the terminal time compared to standalone stabilized FEM solutions.

Keywords: PINN, Finite elements, Convection-dominated, SUPG, Shock-capturing, Deep learning

*Corresponding author

Email addresses: suleyman.cengizci@antalya.edu.tr (Süleyman Cengizci), ougur@metu.edu.tr (Ömür Uğur), natesan@iitg.ac.in (Srinivasan Natesan)

1. Introduction

The mathematical description of physical phenomena in science and engineering heavily relies on (nonlinear) partial differential equations (PDEs). Convection–diffusion–reaction (CDR) equations constitute a particularly important class of PDEs, as they govern the transport and transformation of quantities such as mass, heat, and momentum. Since analytical solutions to such equations—especially when nonlinearities or coupled systems are involved—rarely possess closed-form expressions, computational techniques have become essential. To that end, one typically employs numerical discretization schemes, semi-analytical techniques, machine learning approaches, or any combination thereof to approximate solutions with acceptable accuracy and computational cost.

High-fidelity numerical simulation of CDR-type PDEs demands meticulous treatment of both spatial and temporal discretization. Classical numerical spatial discretization approaches, including finite difference, finite element, and finite volume schemes, tend to produce (node-to-node) spurious oscillations when convection dominates diffusion, thereby degrading the physical reliability of computed solutions. This long-standing difficulty has motivated the development of numerous stabilized formulations over the past several decades. Within the finite element community, the streamline-upwind/Petrov–Galerkin (SUPG) [1–5], Galerkin/least-squares (GLS) [6], and variational multiscale (VMS) [7] methods have gained widespread acceptance as effective stabilization strategies. Despite their success, these techniques may still yield localized nonphysical oscillations near steep gradients, shocks, or thin boundary and internal layers. Shock-capturing (SC) (also called discontinuity-capturing) operators are therefore often appended to further suppress such oscillations in regions of rapid solution variation. A persistent challenge, however, lies in the proper determination of stabilization parameters, which are typically computed element-by-element. Although numerous empirically motivated parameter definitions exist, a universally applicable formulation remains elusive, and parameter tuning can impose a significant computational overhead, particularly for transient and high-dimensional problems. Comprehensive discussions of stabilized finite element techniques and their applications can be found in [8–23] and the references cited therein.

The rapid advancement of deep learning technology has spurred growing interest in its application to PDE solvers. Physics-informed neural networks (PINNs) represent a particularly promising development, wherein physical laws encoded through differential operators are embedded directly into the training loss. By minimizing residuals of the governing equations at selected collocation points, PINNs can approximate solutions without relying on labeled datasets. Nonetheless, PINNs and established numerical methods—including the standard Galerkin finite element method (GFEM)—have largely evolved along separate paths. Recent investigations, however, indicate that machine learning tools, and PINNs in particular, hold considerable promise for augmenting classical solvers by providing data-driven estimates of the artificial dissipation necessary for numerical stability. While various coupling strategies between PINNs and finite element formulations have been explored, the systematic incorporation of shock-capturing mechanisms into continuous FEM-based PINN frameworks has received very limited attention. Addressing this gap could yield improvements in both accuracy and efficiency, and extend the reach of stabilized methods to more demanding applications.

A number of investigations have sought to leverage artificial neural networks (ANNs) for improving the stability and fidelity of conventional numerical schemes. Ray and Hesthaven [24, 25], for example, utilized

multilayer perceptrons to detect oscillatory cells in high-order finite element computations and applied slope limiters locally to mitigate nonphysical behavior. Veiga et al. [26] developed a parameter-free stabilization strategy for hyperbolic conservation laws, training ANNs to pinpoint regions where artificial dissipation is needed; their approach was validated within a discontinuous Galerkin (dGFEM) setting on scalar advection and the Euler system. Discacciati et al. [27] combined ANNs with Runge–Kutta dGFEM solvers to construct a universal artificial viscosity framework capable of maintaining optimal accuracy for smooth solutions while reliably capturing discontinuities. Schwander et al. [28] trained networks to assess local regularity within a Fourier spectral context and benchmarked their method against entropy viscosity approaches on one- and two-dimensional conservation laws as well as the Euler equations.

The foundational work on PINNs by Raissi et al. [29] demonstrated that differential equations can be solved by minimizing residuals at collocation points in an unsupervised or semi-supervised manner, without the need for labeled training data. Karniadakis et al. [30] subsequently broadened this paradigm to encompass high-dimensional inverse problems, scenarios involving noisy observations, and the discovery of latent physics, underscoring the versatility of PINNs for both forward and inverse modeling. Mitusch et al. [31] presented a hybrid FEM–PINN implementation built on the open-source libraries `FEniCS` [32, 33] and `dolfin-adjoint` [34], with applications to Poisson and CDR problems as well as cardiac electrophysiology. Huang et al. [35] provided a taxonomy of deep neural network (DNN) approaches for CDR-type equations along with an assessment of their applicability in scientific and engineering contexts. Jin et al. [36] introduced NSFnets, a PINN architecture tailored for the incompressible Navier–Stokes equations covering both laminar and turbulent regimes.

Yu and Hesthaven [37] constructed a data-driven artificial viscosity model for dGFEM that substantially outperformed classical modal decay indicators in smoothness detection. Yadav and Ganesan [38] proposed SPDE-ConvNet, a convolutional neural network integrated with SUPG stabilization for singularly perturbed CDR equations, demonstrating effective parameter optimization and oscillation suppression. Huang [39] formulated a variationally consistent nodally integrated meshfree method aimed at advection-dominated problems, addressing the loss of Galerkin exactness inherent in nodal integration. Le-Duc et al. [40] developed the finite-element-informed neural network (FEI-NN) for parametric structural mechanics simulations. In subsequent work, Yadav and Ganesan [41] introduced SPDE-NetII, an ANN-augmented SUPG scheme that achieved improved resolution of boundary and interior layers and surpassed the performance of standard PINNs and Variational Neural Networks (VarNet) [42] in benchmark comparisons. Luong et al. [43] addressed the imposition of exact boundary conditions on complex geometries through a two-stage procedure: constructing DNN-based trial functions satisfying homogeneous essential conditions, followed by solution of the resulting boundary value problem.

Grossmann et al. [44] conducted a rigorous comparison between PINNs and FEM for linear and nonlinear PDEs, including the Poisson, Allen–Cahn, and semi-linear Schrödinger equations, concluding that FEM generally attains superior accuracy while PINNs may offer computational advantages in certain settings. Yamazaki et al. [45] integrated weak Galerkin formulations with implicit Euler time stepping to devise Finite Operator Learning (FOL), achieving high accuracy for time-dependent heat conduction in heterogeneous media. Efforts to accelerate training include the Fourier neural operators and Koopman neural networks explored by Buzaev et

al. [46], as well as the curriculum learning strategy of Wang et al. [47], which prioritizes easier subdomains before tackling high-loss regions. Chang et al. [48, 49] proposed singular-layer PINNs (sl-PINNs) that embed boundary layer structure directly into the network architecture, improving performance for singular perturbation problems. Frerichs-Mihov et al. [50] designed specialized loss functions for convection-dominated flows, while Hsieh and Huang [51] developed a multiscale stabilized PINN formulation incorporating weak boundary enforcement, Sobolev training, and transfer learning to enhance stability near boundary layers. Kütük and Yücel [52] embedded the energy dissipation structure of the Allen–Cahn equation into the PINN loss and demonstrated accurate modeling of phase separation and metastability across one to three dimensions. Most recently, Raina et al. [53] tackled two-parameter singular perturbation problems in fluid mechanics, identifying limitations of standard PINNs in resolving boundary layers and proposing finite basis PINNs (FB-PINNs) inspired by finite element methodology.

In the present work, we extend the hybrid framework proposed in [54] by the authors of this current study—termed PASSC (PINN-Augmented SUPG with Shock-Capturing)—originally developed for advection-dominated steady CDR-type PDEs, to the unsteady regime. The main contributions of this study can be summarized as follows. First, we present a hybrid training paradigm that leverages two sophisticated FEM ingredients—SUPG stabilization and the $YZ\beta$ shock-capturing mechanism [55, 56]—to produce high-fidelity training data for unsteady convection-dominated problems exhibiting boundary and/or internal layers. Although SUPG stabilization performs well in many such scenarios, auxiliary shock-capturing is often necessary to adequately resolve sharp gradients and internal discontinuities [57, 58]. Accordingly, we employ SUPG- $YZ\beta$ solutions as training data while selectively imposing PDE residual constraints in stable interior regions. Second, the proposed architecture is dimension-agnostic, featuring deep residual networks with Fourier feature embeddings, layer normalization, and conservative hyperparameter choices. Third, the methodology is inherently scalable, accommodating problems in one, two, and three spatial dimensions.

2. Mathematical Framework

Let $n_{\text{sd}} \geq 1$ denote the spatial dimension, and let $\Omega \subset \mathbb{R}^{n_{\text{sd}}}$ be a bounded Lipschitz domain representing the physical region occupied by the flow, i.e., the spatial domain in which the problem is defined. To establish the mathematical framework addressed in this manuscript, we consider the following time-dependent CDR-type PDE as a representative model problem:

$$\frac{\partial u(t, \mathbf{x})}{\partial t} - \varepsilon \Delta u(t, \mathbf{x}) + \mathbf{b}(t, \mathbf{x}) \cdot \nabla u(t, \mathbf{x}) + c(\mathbf{x})u(t, \mathbf{x}) = f(t, \mathbf{x}) \quad \text{in } \Omega \times (t_0, t_f], \quad (1)$$

$$u(t, \mathbf{x}) = u_D(t, \mathbf{x}) \quad \text{on } \partial\Omega \times (t_0, t_f], \quad (2)$$

$$u(t_0, \mathbf{x}) = u_0(\mathbf{x}) \quad \text{in } \Omega. \quad (3)$$

Here, u denotes the unknown scalar field, where $t \in (t_0, t_f]$ is the temporal variable and $\mathbf{x} = (x_1, x_2, \dots, x_{n_{\text{sd}}}) \in \Omega$ is the spatial position vector. The positive constant ε represents the diffusion coefficient, which is assumed to satisfy $0 < \varepsilon \ll 1$ in convection-dominated regimes. The vector field $\mathbf{b} \in L^\infty([t_0, t_f]; \mathcal{W}^{1,\infty}(\Omega)^{n_{\text{sd}}})$ denotes the convection velocity, $c \in L^\infty(\Omega)$ is the reaction coefficient, and $f \in L^2([t_0, t_f]; L^2(\Omega))$ is the source term.

The function $u_0 \in L^2(\Omega)$ prescribes the initial condition, while $u_D \in C([t_0, t_f]; \mathcal{H}^{1/2}(\partial\Omega))$ specifies the time-dependent Dirichlet boundary data, where $\mathcal{H}^{1/2}(\partial\Omega)$ denotes the trace space of $\mathcal{H}^1(\Omega)$ on $\partial\Omega$, such that for each $t \in [t_0, t_f]$, the function $u_D(t, \cdot)$ admits an extension to $\mathcal{H}^1(\Omega)$. Throughout this work, we adopt standard Sobolev space notation: $L^2(\Omega)$ and $L^\infty(\Omega)$ denote the spaces of square-integrable and essentially bounded functions, respectively; $\mathcal{W}^{1,\infty}(\Omega)$ is the space of functions with essentially bounded first-order weak derivatives; and $\mathcal{H}^1(\Omega)$ denotes the space of functions with square-integrable first-order derivatives. For a Banach space X , the notation $C([t_0, t_f]; X)$ and $L^2([t_0, t_f]; X)$ refers to the standard spaces of continuous and square-integrable X -valued functions, respectively.

Remark 1. Although the governing equations (1)–(3) are equipped with Dirichlet boundary conditions, the proposed framework readily accommodates Neumann-type conditions as well. For brevity and clarity of exposition, we focus exclusively on the Dirichlet case throughout the subsequent development.

Remark 2. For notational convenience in the finite element formulations of Sections 2.1–2.3, the explicit spatial dependence of field quantities is omitted whenever the meaning remains clear from context. Accordingly, the convection velocity $\mathbf{b}(t, \mathbf{x})$, reaction coefficient $c(\mathbf{x})$, and source term $f(t, \mathbf{x})$ are henceforth denoted by \mathbf{b} , c , and f , respectively.

2.1. Standard Galerkin finite element method formulation

The standard Galerkin finite element formulation corresponding to the model problem defined in Eqs. (1)–(3) seeks a solution $u^h \in \mathcal{S}_u^h$ such that for all test functions $w^h \in \mathcal{V}_u^h$:

$$\int_{\Omega} w^h \frac{\partial u^h}{\partial t} d\Omega + \int_{\Omega} (\varepsilon \nabla w^h \cdot \nabla u^h + w^h \mathbf{b} \cdot \nabla u^h + c w^h u^h) d\Omega = \int_{\Omega} w^h f d\Omega. \quad (4)$$

In this formulation, the superscript h denotes membership in a finite-dimensional function space. The discrete trial and test function spaces are defined as:

$$\mathcal{S}_u^h = \{u^h \in \mathcal{H}^{1h}(\Omega) : u^h \doteq u_D^h \text{ on } \partial\Omega\}, \quad (5)$$

$$\mathcal{V}_u^h = \{w^h \in \mathcal{H}^{1h}(\Omega) : w^h \doteq 0 \text{ on } \partial\Omega\}, \quad (6)$$

where u_D^h denotes the discrete representation of the boundary data u_D on the finite element space, and the symbol \doteq indicates that the boundary values are assigned in the sense of the finite element interpolation. The space $\mathcal{H}^{1h}(\Omega)$ denotes a finite-dimensional subspace of the Sobolev space $\mathcal{H}^1(\Omega)$ and is defined by:

$$\mathcal{H}^{1h}(\Omega) = \{\phi^h \in \mathcal{C}^0(\bar{\Omega}) : \phi^h|_{\Omega^e} \in \mathbb{P}_1(\Omega^e), \forall \Omega^e \in \mathcal{T}^h\}. \quad (7)$$

Here, $\mathcal{C}^0(\bar{\Omega})$ represents the space of continuous functions defined over the closure of the computational domain $\bar{\Omega}$. The set $\mathbb{P}_1(\Omega^e)$ denotes the space of piecewise linear polynomial functions defined on each finite element Ω^e , and \mathcal{T}^h represents the mesh partition of the domain into finite elements.

This standard Galerkin formulation serves as a baseline for the numerical treatment of CDR-type PDEs. However, in convection-dominated regimes, it is well known that this approach typically suffers from numerical instabilities and nonphysical oscillations, motivating the need for stabilization techniques such as SUPG and shock-capturing methods discussed in subsequent sections.

2.2. SUPG-stabilized finite element formulation

The SUPG-stabilized finite element formulation corresponding to the model problem in Eqs. (1)–(3) seeks a discrete solution $u^h \in \mathcal{S}_u^h$ such that, for all test functions $w^h \in \mathcal{V}_u^h$:

$$\int_{\Omega} w^h \frac{\partial u^h}{\partial t} d\Omega + \int_{\Omega} (\varepsilon \nabla w^h \cdot \nabla u^h + w^h \mathbf{b} \cdot \nabla u^h + c w^h u^h) d\Omega - \int_{\Omega} w^h f d\Omega + \underbrace{\sum_{e=1}^{n_{\text{el}}} \int_{\Omega^e} \tau_{\text{SUPG}} (\mathbf{b} \cdot \nabla w^h) \left(\frac{\partial u^h}{\partial t} - \varepsilon \Delta u^h + \mathbf{b} \cdot \nabla u^h + c u^h - f \right) d\Omega^e}_{\mathcal{R}(u^h)} = 0. \quad (8)$$

The first integral in formulation (8) corresponds to the standard GFEM formulation, while the second line represents the SUPG contribution. The solution and test function spaces \mathcal{S}_u^h and \mathcal{V}_u^h are identical to those defined in the GFEM formulation. The index n_{el} denotes the number of finite elements in the mesh discretization, and τ_{SUPG} is the stabilization parameter associated with the SUPG formulation.

Remark 3. Throughout this study, all finite element computations employ the continuous piecewise-linear space $\mathcal{H}^1(\Omega)$. Although higher-order polynomial bases (e.g., \mathbb{P}_2 or \mathbb{P}_3) may yield superior accuracy in smooth regions, they incur greater computational costs and can become susceptible to numerical instabilities when convection dominates, especially in the presence of sharp internal layers or steep gradients. Moreover, without adequate stabilization, elevated polynomial degrees tend to amplify spurious oscillations in such regimes. In contrast, linear elements offer reduced assembly and solution times while integrating seamlessly with SUPG stabilization and shock-capturing techniques. Consequently, we deliberately employ stabilized \mathbb{P}_1 elements to achieve an effective compromise between computational efficiency and robustness, thereby facilitating accurate simulations across a wide range of convection-dominated problems.

In formulation (8), the parameter τ_{SUPG} dictates the level of artificial diffusion added to the discrete system for stabilization purposes. Selecting this parameter involves a delicate balance: excessively large values produce over-diffused solutions that compromise accuracy, while values that are too small permit oscillatory artifacts to persist. Thus, careful, problem-dependent tuning of τ_{SUPG} is indispensable. Although the literature offers a variety of robust definitions, no single universally optimal formula has emerged. In this present study, we prefer to adopt the stabilization parameter proposed by Shakib et al. [59], with additional discussion available in [9, 60]:

$$\tau_{\text{SUPG}} = \left(\left(\frac{2}{\Delta t} \right)^2 + \left(\frac{2\|\mathbf{b}\|}{h_K} \right)^2 + \left(\frac{4\varepsilon}{h_K^2} \right)^2 \right)^{-1/2}. \quad (9)$$

Here, $\|\mathbf{b}\|$ denotes the magnitude of the convection velocity (with $\|\cdot\|$ representing the Euclidean norm used consistently throughout this paper), Δt represents the time-step size, and h_K is the characteristic mesh size associated with element $K = \Omega^e$, defined as

$$h_K = \text{diam}(K), \quad \forall K \in \mathcal{T}^h. \quad (10)$$

Remark 4. A key property of the SUPG formulation in Eq. (8) is that the stabilization term incorporates the residual, $\mathcal{R}(u^h)$, of the governing PDE (1) as a weighting factor. This construction ensures consistency: whenever the exact solution is substituted into the formulation, the stabilization contribution vanishes identically.

Extensive numerical evidence [14, 16, 17, 23, 57, 58, 61–65] indicates that the SUPG method, while effective in many scenarios, can be inadequate for suppressing node-to-node oscillations near sharp gradients or shock-like features. To address this shortcoming, supplementary shock-capturing mechanisms are typically required. In the present work, we adopt the $YZ\beta$ shock-capturing technique, originally proposed by Tezduyar and collaborators [55, 56, 66–68], to enhance solution quality in regions exhibiting steep spatial variations.

2.3. SUPG- $YZ\beta$ formulation

The GFEM finite element formulation, augmented with SUPG stabilization and $YZ\beta$ shock-capturing, reads: find $u^h \in \mathcal{S}_u^h$ such that for all $w^h \in \mathcal{V}_u^h$,

$$\begin{aligned} \int_{\Omega} w^h \frac{\partial u^h}{\partial t} d\Omega + \int_{\Omega} \left(\varepsilon \nabla w^h \cdot \nabla u^h + \mathbf{b} \cdot \nabla u^h w^h + c u^h w^h - f w^h \right) d\Omega \\ + \sum_{e=1}^{n_{el}} \int_{\Omega^e} \tau_{\text{SUPG}} (\mathbf{b} \cdot \nabla w^h) \left(\frac{\partial u^h}{\partial t} - \varepsilon \Delta u^h + \mathbf{b} \cdot \nabla u^h + c u^h - f \right) d\Omega \\ + \sum_{e=1}^{n_{el}} \int_{\Omega^e} \nu_{\text{SHOC}} (\nabla w^h \cdot \nabla u^h) d\Omega = 0. \end{aligned} \quad (11)$$

The first line in Eq. (11) represents the standard Galerkin formulation, the second introduces SUPG stabilization terms, and the third includes the shock-capturing term. The function spaces \mathcal{S}_u^h and \mathcal{V}_u^h are defined as previously. The $YZ\beta$ shock-capturing parameter, ν_{SHOC} , can be defined as follows [55, 56, 66–68]:

$$\nu_{\text{SHOC}} = |\mathbf{Y}^{-1} \mathbf{Z}| \left(\sum_{i=1}^{n_{sd}} \left| \mathbf{Y}^{-1} \frac{\partial u^h}{\partial x_i} \right|^2 \right)^{\frac{\beta}{2}-1} \left(\frac{h_{\text{SHOC}}}{2} \right)^{\beta}, \quad (12)$$

where \mathbf{Y} is a scalar representing a reference value of the solution u .

Remark 5. The parameter \mathbf{Y} is a nonzero scaling constant selected to reflect a reference scale of the solution. A typical specification is

$$\mathbf{Y} = \frac{u^{\max} + u^{\min}}{2}, \quad (13)$$

representing the mean of the expected solution range; more generally, any appropriate value between u^{\min} and u^{\max} may be chosen. For transient problems, the initial condition often provides a suitable basis for determining \mathbf{Y} . In the context of coupled systems of equations, \mathbf{Y} is replaced by a diagonal matrix \mathbf{Y} whose entries encode the reference scales for each governing equation; see [61, 68] for further discussion.

The quantity \mathbf{Z} appearing in Eq. (12) represents the pointwise residual of the time-dependent governing equation, expressed following [69] as

$$\mathbf{Z} = \mathcal{R}(u^h) = \frac{\partial u^h}{\partial t} - \varepsilon \Delta u^h + \mathbf{b} \cdot \nabla u^h + c u^h - f. \quad (14)$$

Remark 6. This residual definition extends the original formulation of Tezduyar [55, 56, 66–68] by incorporating all terms from the governing equation. As a consequence, the shock-capturing contribution vanishes identically when the exact solution is attained, thereby avoiding spurious numerical diffusion and ensuring consistency of the formulation. For systems of coupled equations, the scalar \mathbf{Z} generalizes to a residual vector \mathbf{Z} , and in view of Remark 5, the absolute value $|\mathbf{Y}^{-1} \mathbf{Z}|$ is replaced by the norm $\|\mathbf{Y}^{-1} \mathbf{Z}\|$.

Remark 7. The exponent β in Eq. (12) controls the sensitivity of the shock-capturing operator to solution gradients. In particular, $\beta = 1$ is appropriate for moderately sharp transitions, while $\beta = 2$ provides stronger regularization for severely steep gradients. Intermediate values may also be employed, as discussed in [68]. Given that the present work targets strongly convection-dominated problems exhibiting pronounced solution fronts, we adopt $\beta = 2$ throughout.

The shock-capturing length scale, h_{SHOC} , is defined as:

$$h_{\text{SHOC}} = \left[2 \left(\sum_{a=1}^{n_{\text{en}}} |\mathbf{j} \cdot \nabla N_a| \right) \right]^{-1}, \quad \text{with } \mathbf{j} = \frac{\nabla u^h}{\|\nabla u^h\|}, \quad (15)$$

where n_{en} is the number of element nodes, and N_a is the shape function corresponding to node a .

Remark 8. Many shock-capturing formulations define the length scale h_{SHOC} using directionally weighted measures aligned with the local convection field. Despite their potential for improved accuracy, such approaches often require additional mesh-related preprocessing and can complicate implementation. In the present work, we adopt a simpler strategy by setting $h_{\text{SHOC}} = h_K$ (see Eq. (10)), which avoids directional dependence and reduces computational cost. While this approximation may be less precise on strongly anisotropic element configurations, the numerical results presented herein demonstrate that it provides stable and sufficiently accurate predictions across all test cases considered.

Remark 9. Based on the considerations in Remarks 7 and 8, the shock-capturing viscosity ν_{SHOC} in Eq. (12) simplifies to

$$\nu_{\text{SHOC}} = \frac{|Y^{-1}Z| h_K^2}{4}. \quad (16)$$

As with the SUPG stabilization parameter, selecting an appropriate value for ν_{SHOC} remains a challenging and inherently problem-specific task. In practice, this coefficient is often determined through empirical calibration or heuristic tuning. This difficulty highlights the appeal of data-driven methodologies such as PINNs, which can learn and adjust stabilization parameters directly from physical constraints and available data. Beyond parameter estimation, PINNs can serve as post-processing correctors that refine stabilized finite element solutions by minimizing residuals derived from the governing equations and boundary/initial conditions. This capability is examined in detail in the following section.

Remark 10. The finite element component of the proposed hybrid methodology is not limited to the particular stabilization and shock-capturing schemes employed here. Other stabilized formulations, including GLS or VMS, can be seamlessly integrated into the framework. Likewise, alternative shock-capturing operators or spurious oscillations at layers diminishing (SOLD) methods may replace the $YZ\beta$ technique adopted in this work. The choice of SUPG stabilization combined with $YZ\beta$ shock-capturing is motivated primarily by the authors' prior experience with these approaches in the context of convection-dominated transport problems.

3. Integration of PINNs with SUPG- $YZ\beta$ Formulation

Following the framework introduced for steady-state problems in [54], this section presents the hybrid computational strategy that couples stabilized finite element approximations with physics-informed neural

networks. The network architecture, together with the multi-phase training procedure, is depicted in Figures 1 and 2.

Remark 11. Although the proposed framework applies to CDR-type problems in one, two, or three spatial dimensions, all formulations and algorithmic descriptions are presented for the two-dimensional setting ($n_{\text{sd}} = 2$) unless stated otherwise. This convention is adopted for notational simplicity and readability; the generalization to other dimensions is straightforward.

3.1. Motivation for Hybrid PINN-FEM Integration

Coupling PINNs with the SUPG-YZ β formulation mitigates key shortcomings that arise when either method is applied standalone. The SUPG-YZ β approach, though numerically robust, depends on user-specified parameters whose optimal values are generally determined through empirical rules or case-by-case calibration, potentially limiting performance across varying flow scenarios. Conversely, conventional PINNs, despite their conceptual elegance, frequently encounter difficulties in resolving thin boundary layers and may suffer from prolonged training times in strongly convection-dominated settings. The proposed hybrid strategy overcomes these obstacles through several innovations. Numerically stable SUPG-YZ β solutions provide informative priors, allowing the neural network to concentrate on resolving fine-scale features rather than learning fundamental PDE behavior from the outset. Simultaneously, the framework exploits the stability of SUPG-YZ β discretizations to accelerate convergence while retaining the representational flexibility of PINNs for complex physical phenomena. This constitutes the principal contribution of the present study relative to existing FEM-PINN coupling strategies (see, e.g., [31, 40, 41]): by anchoring network training in stabilized finite element solutions, the methodology inherits the robustness of classical numerical schemes while benefiting from the adaptability of data-driven learning.

3.2. Network Architecture and Fourier Feature Mapping

The PINN architecture employs random Fourier feature mapping to enhance the network’s ability to capture high-frequency variations characteristic of boundary layers and internal shocks. Given spatiotemporal input coordinates $\mathbf{z} = (t, \mathbf{x}) \in \mathbb{R}^{n_{\text{sd}}+1}$, the Fourier feature embedding is defined as:

$$\phi(\mathbf{z}) = \begin{bmatrix} \mathbf{z} \\ \sin(\mathbf{B}^\top \mathbf{z}) \\ \cos(\mathbf{B}^\top \mathbf{z}) \end{bmatrix} \in \mathbb{R}^{n_{\text{sd}}+1+2n_{\text{F}}}, \quad (17)$$

where $\mathbf{B} \in \mathbb{R}^{(n_{\text{sd}}+1) \times n_{\text{F}}}$ is a random frequency matrix whose entries are independently sampled from a normal distribution $\mathcal{N}(0, \sigma^2)$ and held fixed (i.e., not trained) throughout optimization. Here, n_{F} denotes the number of Fourier features and σ controls the frequency bandwidth. The trigonometric functions are applied element-wise to the projection $\mathbf{B}^\top \mathbf{z} \in \mathbb{R}^{n_{\text{F}}}$, and the resulting feature vector $\phi(\mathbf{z})$ concatenates the raw coordinates with the sine and cosine projections.

The Fourier-enhanced features are first mapped to a hidden dimension n_h through an input layer:

$$\mathbf{h}_0 = \text{SiLU}\left(\mathbf{W}^{(0)}\phi(\mathbf{z}) + \tilde{\mathbf{b}}^{(0)}\right), \quad (18)$$

where $\mathbf{W}^{(0)} \in \mathbb{R}^{n_h \times (n_{sd} + 1 + 2n_F)}$ and $\tilde{\mathbf{b}}^{(0)} \in \mathbb{R}^{n_h}$. The network then processes this representation through n_r residual blocks, each of which transforms the hidden state according to:

$$\mathbf{p}_i = \text{SiLU}(\text{Linear}_1(\mathbf{h}_i)), \quad (19)$$

$$\mathbf{q}_i = \text{Linear}_2(\mathbf{p}_i), \quad (20)$$

$$\mathbf{h}_{i+1} = \text{SiLU}(\text{LayerNorm}(\mathbf{q}_i + \mathbf{h}_i)), \quad (21)$$

where $\mathbf{h}_i \in \mathbb{R}^{n_h}$ denotes the hidden state at the i -th block for $i = 0, 1, \dots, n_r - 1$. Here, Linear_1 and Linear_2 denote standard fully connected (affine) transformations of the form

$$\text{Linear}(\mathbf{v}) = \mathbf{W}\mathbf{v} + \tilde{\mathbf{b}}, \quad (22)$$

with trainable weight $\mathbf{W} \in \mathbb{R}^{n_h \times n_h}$ and bias $\tilde{\mathbf{b}} \in \mathbb{R}^{n_h}$; each residual block uses two such layers with distinct parameter sets. The skip connection $\mathbf{q}_i + \mathbf{h}_i$ followed by layer normalization mitigates gradient degradation in deep architectures. The specific hyperparameter values (n_h, n_r, n_F, σ) adopted for each numerical experiment are reported in Section 5.

The SiLU (sigmoid-weighted linear unit, Swish) activation function is defined as:

$$\text{SiLU}(x) = x \cdot \text{sigmoid}(x) = \frac{x}{1 + e^{-x}}. \quad (23)$$

This smooth, non-monotonic activation promotes better gradient flow compared to ReLU (rectified linear unit)-based alternatives and has demonstrated superior performance in physics-informed learning tasks, particularly for problems involving smooth solution variations. LayerNorm provides training stability through normalization:

$$\text{LayerNorm}(\mathbf{x}) = \frac{\mathbf{x} - \mu_{\text{LN}}}{\sqrt{\sigma_{\text{LN}}^2 + \epsilon_{\text{LN}}}} \odot \boldsymbol{\gamma}_{\text{LN}} + \boldsymbol{\beta}_{\text{LN}}, \quad (24)$$

where μ_{LN} and σ_{LN}^2 are the mean and variance computed over the feature dimension, $\boldsymbol{\gamma}_{\text{LN}}$ and $\boldsymbol{\beta}_{\text{LN}}$ are learnable scale and shift parameters, respectively, ϵ_{LN} is a small constant for numerical stability, and \odot denotes the element-wise (Hadamard) product.

3.3. Data-driven Training Approach

Using the numerically stable FEM approximations obtained by employing the SUPG-YZ β formulation, we train the PINN model with the mean squared error data loss function:

$$\mathcal{L}_{\text{data}}(\theta) = \frac{1}{K_s} \sum_{k=1}^{K_s} \left[\frac{1}{N_h} \sum_{i=1}^{N_h} |u_{\text{NN}}(t_k, \mathbf{x}_i; \theta) - u_{\text{SUPG-YZ}\beta}^h(t_k, \mathbf{x}_i)|^2 \right], \quad (25)$$

where K_s denotes the number of temporal snapshots selected near the terminal time and N_h is the number of nodal vertices in the finite element mesh \mathcal{T}^h , yielding a total of $N = K_s \times N_h$ space-time training pairs. For each snapshot t_k , the inner sum computes the spatial mean squared error over all mesh nodes $\{\mathbf{x}_i\}_{i=1}^{N_h}$, and the outer sum averages these snapshot-wise errors over the K_s selected time levels. The spatiotemporal coordinates (t_k, \mathbf{x}_i) correspond to the FEM solution evaluated at discrete time levels t_k and mesh nodes \mathbf{x}_i . The term

$u_{\text{NN}}(t_k, \mathbf{x}_i; \theta)$ represents the neural network prediction, $u_{\text{SUPG-YZ}\beta}^h(t_k, \mathbf{x}_i)$ is the corresponding stabilized FEM solution, and θ denotes the trainable network parameters. This loss function enforces the neural network to learn the spatiotemporal evolution and boundary layer structures captured by the stabilized finite element method. The data-driven approach offers several advantages: (i) it leverages the computational expertise embedded in mature FEM solvers, (ii) it avoids the challenges associated with balancing multiple loss terms in purely physics-informed training, and (iii) it ensures that the learned solution inherits the stability properties of the underlying SUPG-YZ β formulation.

Remark 12. The selective enforcement strategy detailed in Section 3.5 applies exclusively to the PDE residual loss $\mathcal{L}_{\text{pde}}(\theta)$, which is computed only at interior collocation points. Both the data loss $\mathcal{L}_{\text{data}}(\theta)$ and the boundary loss $\mathcal{L}_{\text{bc}}(\theta)$ are computed over their complete respective point sets without any distance-based or selective filtering: $\mathcal{L}_{\text{data}}$ utilizes all $N = K_s \times N_h$ space-time points to maintain global solution fidelity, while \mathcal{L}_{bc} employs all boundary nodes on $\partial\Omega$.

3.4. Hybrid Physics-informed Training with Selective Enforcement

To incorporate physical constraints while maintaining data fidelity, we propose a multiphase hybrid training strategy with selective physics enforcement. This approach recognizes that not all regions of the computational domain are equally suitable for physics-based learning. The hybrid loss function combines weighted components, for example:

$$\mathcal{L}_{\text{hybrid}}(\theta) = w_{\text{data}}\mathcal{L}_{\text{data}}(\theta) + w_{\text{pde}}\mathcal{L}_{\text{pde}}(\theta) + w_{\text{bc}}\mathcal{L}_{\text{bc}}(\theta), \quad (26)$$

where each component is to be defined below, and the nonnegative scalar weights $w_{\text{data}}, w_{\text{pde}}, w_{\text{bc}}$ control the relative importance of data consistency, PDE residual minimization, and boundary condition enforcement, respectively.

Remark 13. These weights serve as balancing factors to tune the contribution of each term to the overall training objective. The dynamic evolution of these weights throughout training enables a curriculum learning approach, where the network first learns to approximate the reference solution before gradually incorporating physical constraints. This prevents early training instabilities that can arise when physics terms dominate before a basic solution approximation is established.

The PDE residual loss enforces the governing CDR-type equation over randomly sampled interior collocation points:

$$\mathcal{L}_{\text{pde}}(\theta) = \frac{1}{N_{\text{int}}} \sum_{j=1}^{N_{\text{int}}} |\mathcal{R}^{\text{NN}}(t_j, \mathbf{x}_j; \theta)|^2, \quad (27)$$

where the interior collocation set is defined as

$$\mathcal{X}_{\text{int}} = \{(t_j, \mathbf{x}_j) \in [t_{\text{start}}, t_{\text{end}}] \times \Omega : d_{\partial\Omega}(\mathbf{x}_j) > d_{\text{min}}\}. \quad (28)$$

Here, the spatiotemporal collocation points (t_j, \mathbf{x}_j) are drawn uniformly at random within the training time window $[t_{\text{start}}, t_{\text{end}}]$ and the spatial domain Ω , and $d_{\partial\Omega}(\mathbf{x})$ denotes the Euclidean distance from point \mathbf{x} to the nearest boundary $\partial\Omega$. The threshold parameter d_{min} controls the exclusion zone near boundaries where PDE

residuals are not enforced; its value is problem-dependent and should be chosen based on the expected boundary layer thickness and mesh resolution (see Section 3.5.1 for details). The term N_{int} denotes the number of interior collocation points that satisfy the distance criterion. The strong-form PDE residual \mathcal{R}^{NN} for the PINNs is defined as:

$$\mathcal{R}^{\text{NN}}(t, \mathbf{x}; \theta) = \frac{\partial u_{\text{NN}}}{\partial t} - \varepsilon \Delta u_{\text{NN}} + \mathbf{b}(t, \mathbf{x}) \cdot \nabla u_{\text{NN}} + c(\mathbf{x}) u_{\text{NN}} - f(t, \mathbf{x}), \quad (29)$$

where $u_{\text{NN}} = u_{\text{NN}}(t, \mathbf{x}; \theta)$ and all partial derivatives are computed via automatic differentiation with respect to the spatiotemporal input coordinates. The temporal derivative $\partial u_{\text{NN}}/\partial t$ is obtained entirely through automatic differentiation, eliminating the need for finite-difference approximations or access to the FEM solution at adjacent time steps.

The boundary condition loss enforces the Dirichlet condition $u = u_D$ on $\partial\Omega$ by penalizing deviations of the neural network prediction from the prescribed boundary values:

$$\mathcal{L}_{\text{bc}}(\theta) = \frac{1}{N_{\text{bc}}} \sum_{k=1}^{N_{\text{bc}}} |u_{\text{NN}}(t_k, \mathbf{x}_k; \theta) - u_D(t_k, \mathbf{x}_k)|^2, \quad (30)$$

where $\mathbf{x}_k \in \partial\Omega$ are collocation points distributed uniformly along each edge of the domain boundary, $t_k \in [t_{\text{start}}, t_{\text{end}}]$ are sampled at discrete time levels within the training window, and $u_D(t_k, \mathbf{x}_k)$ denotes the prescribed Dirichlet data, which may in general depend on both space and time. The total number of boundary collocation points is $N_{\text{bc}} = N_{\text{sides}} \times N_{\text{pts}} \times N_{\text{times}}$, where N_{sides} is the number of boundary edges, N_{pts} is the number of points per edge, and N_{times} is the number of sampled time levels.

Remark 14. The number of temporal levels used for the boundary condition loss, N_{times} , need not coincide with the number of snapshots K_s employed in the data loss $\mathcal{L}_{\text{data}}(\theta)$. In the data loss (Eq. (25)), K_s denotes the number of FEM solution snapshots selected near the terminal time, each contributing N_h spatial training points. In the boundary loss (Eq. (30)), N_{times} controls the temporal sampling density along the boundary and may be chosen independently of K_s to balance boundary fidelity against computational cost. In particular, since boundary data are typically smooth or piecewise constant in time, a smaller value of N_{times} often suffices.

Remark 15. When the network architecture incorporates a lift function u_{lift} and a distance function $d(\mathbf{x}) = x_1(1 - x_1)x_2(1 - x_2)$ such that the output takes the form

$$u_{\text{NN}}(t, \mathbf{x}; \theta) = u_{\text{lift}}(t, \mathbf{x}) + d(\mathbf{x}) \mathcal{N}(t, \mathbf{x}; \theta), \quad (31)$$

the Dirichlet conditions are satisfied exactly by construction, since $d(\mathbf{x}) = 0$ on $\partial\Omega$ implies $u_{\text{NN}} = u_{\text{lift}} = u_D$ on the boundary. In this case, $\mathcal{L}_{\text{bc}} \equiv 0$ and the boundary loss term can be omitted from the training objective. This lift-based enforcement is applicable when the boundary data u_D is sufficiently smooth; for problems with discontinuous or piecewise-defined boundary conditions, the explicit penalty formulation (30) is employed instead.

Remark 16. The present framework employs soft boundary condition enforcement via $\mathcal{L}_{\text{bc}}(\theta)$ rather than hard enforcement techniques, such as the unified PINN approach of Luong et al. [43], where the network output is algebraically constrained to satisfy essential boundary conditions exactly through trial functions. While hard enforcement eliminates the need for tuning w_{bc} and guarantees exact Dirichlet satisfaction, soft enforcement is

preferred here for several reasons: (i) it provides flexibility in balancing competing objectives during multi-phase training transitions; (ii) the selective physics enforcement strategy excludes boundary-adjacent regions from PDE residual computation, and a separate boundary loss allows explicit control over boundary condition fidelity in these zones; (iii) since SUPG- $YZ\beta$ solutions already satisfy boundary conditions by construction, boundary data is implicitly learned through $\mathcal{L}_{\text{data}}(\theta)$, making $\mathcal{L}_{\text{bc}}(\theta)$ serve primarily as a regularization mechanism during physics-dominant training phases.

3.5. Enhanced Selective Physics Enforcement Strategy

The key innovation lies in the selective application of physics constraints, which addresses a fundamental challenge in hybrid PINN training—determining where and when to apply physics-based learning. Instead of enforcing the PDE residuals uniformly over the entire domain, we adopt a multi-criteria selection strategy that limits physics enforcement to regions where it is most effective. The overall procedure is summarized in Figure 1.

3.5.1. Distance-based Selection Criterion

We introduce a distance function that measures the proximity of a point $\mathbf{x} \in \Omega$ to the boundary $\partial\Omega$ for a rectangular domain $\Omega = [a, b]^2$:

$$d_{\text{boundary}}(\mathbf{x}) = \min_i \left\{ \frac{x_i - a}{b - a}, \frac{b - x_i}{b - a} \right\}, \quad (32)$$

where the minimum is taken over all spatial coordinates. This computes the minimum normalized distance to any boundary face, where each term represents the distance to the nearest boundary in the i -th coordinate direction, scaled by the domain width $(b - a)$. We apply the following distance criterion:

$$d_{\text{boundary}}(\mathbf{x}) > d_{\text{min}}, \quad (33)$$

where d_{min} is chosen such that an optimal balance between physics enforcement and boundary layer preservation is achieved. This selective enforcement ensures that only interior points satisfying the distance criterion contribute to the PDE residual loss $\mathcal{L}_{\text{pde}}(\theta)$, thereby enhancing numerical stability and preserving boundary integrity.

Remark 17. The threshold parameter d_{min} is defined as a normalized quantity relative to a characteristic length scale L of the domain. For a general bounded domain $\Omega \subset \mathbb{R}^n$, let

$$d(\mathbf{x}, \partial\Omega) = \inf_{\mathbf{y} \in \partial\Omega} \|\mathbf{x} - \mathbf{y}\|_2 \quad (34)$$

denote the Euclidean distance from a point $\mathbf{x} \in \Omega$ to the boundary $\partial\Omega$. The normalized distance is then defined as

$$\tilde{d}(\mathbf{x}) = \frac{d(\mathbf{x}, \partial\Omega)}{L}. \quad (35)$$

For rectangular domains $\Omega = [0, L_1] \times [0, L_2] \times \cdots \times [0, L_n]$, the characteristic length is $L = \max_{1 \leq i \leq n} L_i$, and the distance simplifies to

$$d(\mathbf{x}, \partial\Omega) = \min_{1 \leq i \leq n} \min(x_i, L_i - x_i). \quad (36)$$

The selective enforcement condition $\tilde{d}(\mathbf{x}) > d_{\text{min}}$ ensures scale-invariant behavior across problems with different domain sizes. For the unit domains employed in our numerical examples ($L = 1$), the normalized and absolute distances coincide.

3.5.2. Implementation Details and Computational Considerations

The selective physics enforcement is implemented through an efficient masking operation based on the actual code implementation:

$$\mathcal{S}_{\text{physics}}(\mathbf{x}) = \mathbb{I}_{d_{\text{boundary}}(\mathbf{x}) > d_{\text{min}}}, \quad \text{provided that } N_{\text{int}} \geq N_{\text{int}}^{\text{min}}, \quad (37)$$

where the indicator function $\mathbb{I}_{d_{\text{boundary}}(\mathbf{x}) > d_{\text{min}}}$ selects interior points satisfying the distance criterion, and the global condition $N_{\text{int}} \geq N_{\text{int}}^{\text{min}}$ ensures a minimum number of interior points for stable PDE loss computation.

The identification of boundary points is performed using a vectorized distance computation. For a unit square domain $[0, 1]^2$:

$$d_{\text{left}} = x_1, \quad d_{\text{right}} = 1 - x_1, \quad (38)$$

$$d_{\text{bottom}} = x_2, \quad d_{\text{top}} = 1 - x_2, \quad (39)$$

$$d_{\text{boundary}} = \min(d_{\text{left}}, d_{\text{right}}, d_{\text{bottom}}, d_{\text{top}}). \quad (40)$$

Remark 18. Equations (38)–(40) are specific to the unit square domain $\Omega = [0, 1]^2$ employed in the numerical examples. For a general rectangular domain $\Omega = [0, L_1] \times [0, L_2]$, these expressions generalize to $d_{\text{left}} = x_1$, $d_{\text{right}} = L_1 - x_1$, $d_{\text{bottom}} = x_2$, $d_{\text{top}} = L_2 - x_2$, and the normalized distance is $\tilde{d}(\mathbf{x}) = d_{\text{boundary}}/L$ with $L = \max(L_1, L_2)$, as detailed in Remark 17.

The number of PDE collocation points, N_{pde} , is a problem-dependent hyperparameter whose value is selected to balance computational cost with adequate physics sampling density. In general, N_{pde} should be chosen large enough to ensure sufficient coverage of the interior domain—particularly in problems featuring thin layers or steep gradients—while remaining small enough to avoid excessive computational overhead from second-order automatic differentiation. The specific values adopted for each test case are reported alongside the corresponding numerical examples in Section 5. Similarly, the boundary exclusion threshold d_{min} and the minimum interior point count $N_{\text{int}}^{\text{min}}$ (see Eq. (37)) are problem-dependent parameters; their values for each test case are reported in Section 5.

3.6. Multi-phase Weight Evolution

To balance data fidelity with physics enforcement throughout the training process, we implement an adaptive weighting strategy in which the relative importance of each loss term evolves based on training progress. The relative weights assigned to the data loss $\mathcal{L}_{\text{data}}$, PDE residual loss \mathcal{L}_{pde} , and boundary loss \mathcal{L}_{bc} evolve dynamically through distinct phases based on the training progress, e.g.,:

$$\text{Phase I (Data-dominant): } w_{\text{data}} = w_{\text{data}}^{\text{I}}, \quad w_{\text{pde}} = w_{\text{pde}}^{\text{I}}, \quad w_{\text{bc}} = w_{\text{bc}}^{\text{I}}, \quad (41)$$

$$\text{Phase II (Transition): } w_{\text{data}} = w_{\text{data}}^{\text{II}}, \quad w_{\text{pde}} = w_{\text{pde}}^{\text{II}}, \quad w_{\text{bc}} = w_{\text{bc}}^{\text{II}}, \quad (42)$$

$$\text{Phase III (Physics-dominant): } w_{\text{data}} = w_{\text{data}}^{\text{III}}, \quad w_{\text{pde}} = w_{\text{pde}}^{\text{III}}, \quad w_{\text{bc}} = w_{\text{bc}}^{\text{III}}, \quad (43)$$

where the superscripts of weights indicate the phase associated with them.

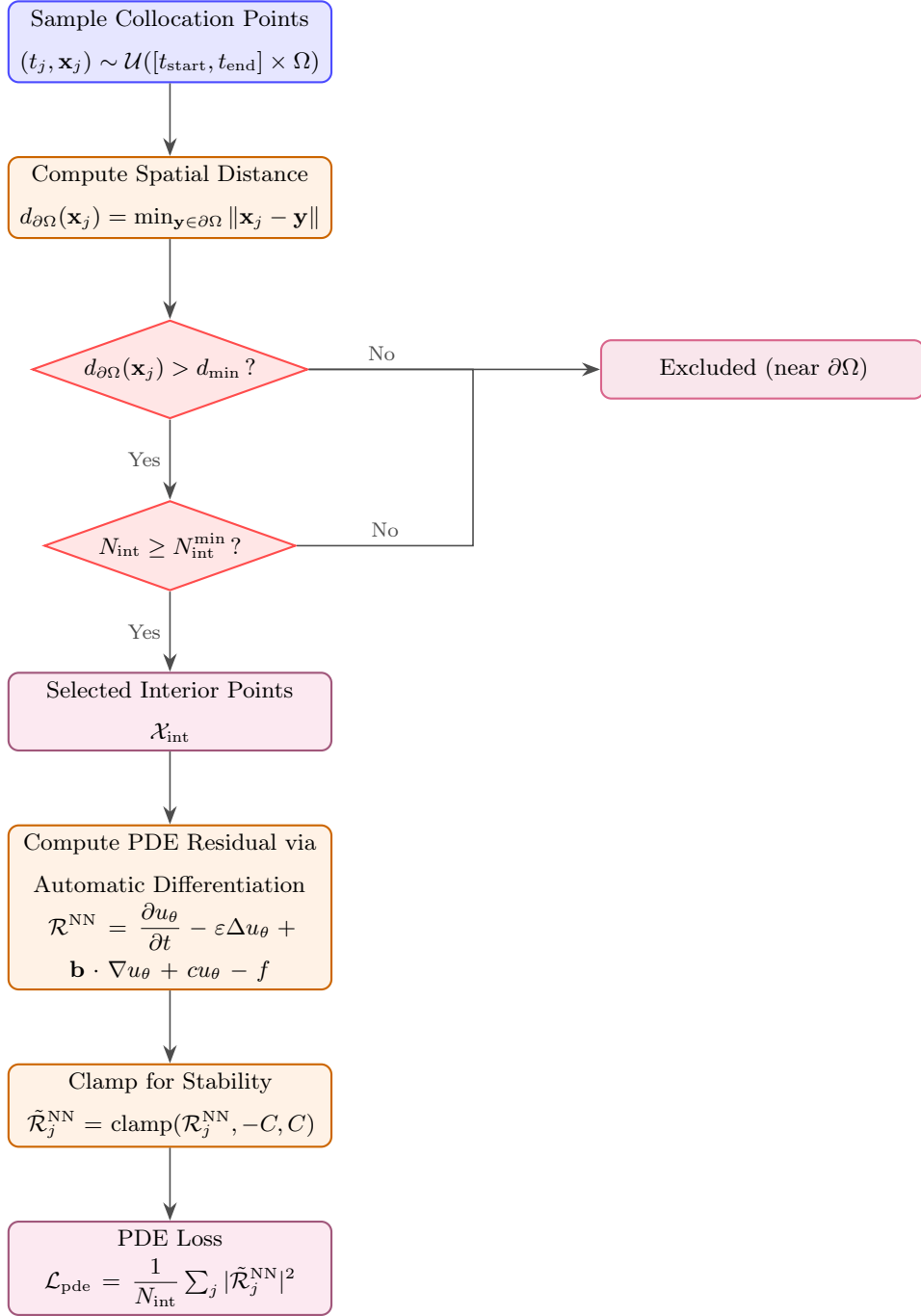


Figure 1: Flowchart illustrating the selective physics enforcement strategy. At each training iteration, spatiotemporal collocation points (t_j, \mathbf{x}_j) are sampled uniformly at random within the training time window and spatial domain. Only points whose spatial distance to the boundary satisfies $d_{\partial\Omega}(\mathbf{x}_j) > d_{\min}$ and for which the minimum count criterion $N_{\text{int}} \geq N_{\text{int}}^{\min}$ holds are retained for PDE residual computation. Boundary-adjacent points are excluded to preserve numerical stability near sharp gradients. The strong-form residual, including the temporal derivative $\partial u_\theta / \partial t$ obtained via automatic differentiation, is clamped to $[-C, C]$ before computing the loss to prevent gradient explosion.

The phase boundaries and loss-weight selections (see Eqs. (41)–(43)) to be used are selected based on numerical experiments. For example, in one-dimensional CDR problems, approximately 1000 – 2000 total epochs can be sufficient for stable and accurate convergence, whereas two-dimensional cases typically require around 2500 – 5000 epochs. These values should, therefore, be interpreted as empirically informed guidelines rather than universally optimal hyperparameters, and may need adjustment for other PDEs or geometries. While more principled dynamic weighting strategies—such as gradient-norm balancing or uncertainty-based scaling—have recently been explored in the broader PINN literature, our empirically-tuned three-phase approach proved robust across all benchmark problems considered. Integrating such adaptive mechanisms into hybrid FEM–PINN frameworks represents a promising direction for future research that could potentially enhance the method’s generalizability.

The rationale behind this progressive strategy is threefold: (i) initializing with data-dominant learning prevents early training instabilities that arise when physics terms dominate before a reasonable solution approximation is established; (ii) the gradual transition allows the network to smoothly adapt to the changing optimization landscape; and (iii) physics-dominant refinement in the final phase enables the hybrid approach to potentially improve upon the FEM reference solution by enforcing the governing PDE directly. The specific weight values for each phase are problem-dependent and will be reported in the numerical examples.

3.7. FEM-PINN Data Transfer and Computational Interface

The seamless integration between `FEniCS` and `PyTorch` is achieved through a carefully designed data transfer protocol that maintains numerical accuracy while enabling efficient GPU-accelerated training. Spatial coordinates $\{\mathbf{x}_i\}_{i=1}^N$ are extracted from the FEM mesh using `FEniCS` function space mappings via `V.tabulate_dof_coordinates()`, and paired with snapshot times $\{t_k\}_{k=1}^{K_s}$ to construct space-time training tuples $\{(t_k, \mathbf{x}_i, u_{\text{SUPG-YZ}\beta}^k(\mathbf{x}_i))\}$. This ensures exact correspondence between finite element nodes and the points used for loss computation across multiple time levels. High-accuracy evaluation of $u_{\text{SUPG-YZ}\beta}^k(\mathbf{x})$ at each snapshot is performed using `FEniCS`’s built-in point evaluation capabilities, maintaining the accuracy of the finite element approximation. Efficient detection of boundary points using spatial tolerance $\epsilon_{\text{boundary}} = 10^{-8}$ and geometric proximity tests are employed.

The hybrid framework leverages `PyTorch`’s automatic differentiation capabilities for computing space-time PDE residuals. The network accepts three-dimensional input (t, x_1, x_2) and produces a scalar output $u_{\text{NN}}(t, x_1, x_2)$. The temporal derivative $\partial u_{\text{NN}}/\partial t$ and spatial gradients ∇u_{NN} are computed simultaneously using `torch.autograd.grad` with `create_graph=True`, enabling higher-order differentiation through the same computational graph. The Laplacian Δu_{NN} is obtained through successive differentiation of spatial first derivatives. The strong-form PDE residual, \mathcal{R}^{NN} , is evaluated at randomly sampled interior collocation points within the training time window $[t_{\text{start}}, t_{\text{end}}]$, with boundary-proximal points excluded via a distance mask ($d > 0.02$) to avoid interference with the explicit boundary condition loss. Efficient batched computation of all derivatives across multiple collocation points leverages GPU parallelization.

3.8. Optimization Strategy and Training Configuration

Training is performed using the `AdamW` stochastic optimization algorithm [70], adopted for its improved generalization capabilities and decoupled weight decay mechanism compared to standard `Adam` [71]. The optimizer

is configured with momentum parameters $\beta_1 = 0.9$, $\beta_2 = 0.999$, and a weight decay coefficient of $\lambda = 10^{-7}$, which serves as implicit L^2 regularization to prevent overfitting and promote smoother solution profiles—particularly beneficial for interior layer problems where solution regularity is crucial.

The initial learning rate is scaled according to the batch size following a square-root scaling rule:

$$\alpha = 8 \times 10^{-5} \times \sqrt{\frac{B}{256}}, \quad (44)$$

where B denotes the mini-batch size. This scaling heuristic maintains stable gradient variance across different batch configurations and prevents oscillations when different loss components have conflicting gradient directions—a phenomenon amplified in the time-dependent setting where the temporal derivative introduces an additional source of gradient competition.

A `ReduceLROnPlateau` scheduler monitors the epoch-averaged total loss and reduces the learning rate by a multiplicative factor $\gamma = 0.9$ after 150 epochs of stagnation, with a minimum learning rate floor of $\alpha_{\min} = 10^{-6}$. The extended patience period accommodates the inherent variability in physics-informed loss landscapes, where temporary plateaus often precede significant improvements as the network learns to balance multiple objectives. The multiplicative decay $\alpha \leftarrow \gamma\alpha$ provides a gradual annealing that preserves training momentum while enabling fine-grained convergence in later epochs.

3.8.1. Gradient Stabilization and Numerical Safeguards

To ensure gradient stability and suppress numerical divergence during training, we implement comprehensive numerical safeguards at three levels: gradient, loss, and residual.

Gradient clipping is applied with a maximum norm constraint $\|\nabla_{\theta}\mathcal{L}\|_2 \leq 1.0$, preventing catastrophic parameter updates in regions of sharp solution gradients where second-order derivatives may become large. A vectorized gradient validation mechanism inspects the concatenated parameter gradient tensor at each optimization step:

$$\text{if } \neg \text{isfinite}\left(\bigoplus_{l=1}^L \nabla_{\theta_l} \mathcal{L}\right) \text{ then discard update and increment NaN counter,} \quad (45)$$

where \bigoplus denotes concatenation across all L parameter groups. Training is terminated if the cumulative NaN count exceeds 10, indicating persistent numerical instability. At the loss level, individual components are similarly guarded:

$$\text{if } \text{isnan}(\mathcal{L}_{\text{hybrid}}) \text{ or } \text{isinf}(\mathcal{L}_{\text{hybrid}}) \text{ then } \mathcal{L}_{\text{hybrid}} \leftarrow \mathcal{L}_{\text{data}}, \quad (46)$$

ensuring that training can recover from transient PDE residual spikes by falling back to the data fidelity loss alone.

Additionally, value clipping via the `clamp(x, a, b)` function is employed to truncate extreme values at multiple stages of the computation:

$$\text{Residual clipping: } \mathcal{R}^{\text{NN}}(\mathbf{x}) \leftarrow \text{clamp}(\mathcal{R}^{\text{NN}}(\mathbf{x}), -10.0, 10.0), \quad (47)$$

$$\text{Loss clipping: } \mathcal{L}_{\text{hybrid}} \leftarrow \text{clamp}(\mathcal{L}_{\text{hybrid}}, 0.0, 100.0), \quad (48)$$

where the `clamp` function is defined as:

$$\text{clamp}(x, a, b) = \begin{cases} a, & \text{if } x < a, \\ x, & \text{if } a \leq x \leq b, \\ b, & \text{if } x > b. \end{cases} \quad (49)$$

The residual clipping bounds of ± 10.0 are chosen to suppress outlier contributions from collocation points near sharp layers while retaining physically meaningful gradient information.

3.8.2. Batch Processing and Mixed-Precision Training

All training data—comprising $K_s \times N_h$ space-time tuples—are preloaded entirely onto the GPU at initialization to eliminate host-to-device transfer overhead. Epoch-level shuffling is performed via in-place random permutation on the device using `torch.randperm`, yielding $\lceil N_{\text{data}}/B \rceil$ mini-batches per epoch, each receiving a full optimizer update. PDE residual evaluation is performed periodically during each epoch rather than at every mini-batch, thereby amortizing the computationally expensive second-order automatic differentiation over multiple data batches. In the default configuration, the residual is computed on the first mini-batch of every epoch; however, this frequency is treated as a tunable parameter and may be adjusted on a per-problem basis—for instance, evaluating the residual every k -th mini-batch when a higher physics sampling rate is beneficial or when the per-batch cost must be further reduced. The specific evaluation frequency adopted for each test case is reported in Section 5. In all cases, N_{pde} collocation points are randomly sampled within the training time window $[t_{\text{start}}, t_{\text{end}}] \times \Omega$ at each evaluation instance.

On CUDA-enabled devices, mixed-precision training via Automatic Mixed Precision (AMP) is selectively applied: the data fidelity and boundary condition forward passes execute in `float16` arithmetic for computational throughput, while PDE residual computations involving higher-order automatic differentiation are maintained in full `float32` precision to preserve the numerical accuracy of second-derivative calculations. A dynamic `GradScaler` adjusts the loss scaling factor to prevent gradient underflow in reduced precision. The best model state, determined by the minimum epoch-averaged total loss, is maintained in CPU memory and checkpointed to disk every 100 epochs for fault tolerance. Training proceeds for $N_{\text{epochs}} = 5000$ epochs across all test cases considered in this work.

3.9. Hyperparameter Selection

The network architecture employs n_r residual blocks with hidden dimension n_h and n_F random Fourier features at scale σ ; the specific values adopted for each test problem are reported in Section 5. Across all examples, the architectural capacity is chosen to balance representational power against overfitting risk: too few parameters would struggle to resolve sharp interfaces, while substantially larger networks would risk memorizing FEM data without learning the underlying physics. The Fourier feature embedding provides the spectral bias correction necessary for representing high-frequency layer structures [72].

Training utilizes the last K_s temporal snapshots from the SUPG- $YZ\beta$ solution, covering a time window $[t_{\text{start}}, t_{\text{end}}] \subset [0, t_f]$ near the terminal time. This windowed approach focuses the PINN’s corrective capacity on

the near-terminal dynamics where advected fronts have developed their most challenging features, while providing sufficient temporal context for the network to learn meaningful $\partial u/\partial t$ behavior through automatic differentiation. The total training dataset comprises $K_s \times N_h$ space–time points; the values of K_s and the batch size B are problem-dependent and are specified alongside each numerical example.

For problems with homogeneous Dirichlet data, the lift-based distance function enforcement described in Remark 15 renders the boundary loss unnecessary ($w_{bc} = 0$). When the boundary data is piecewise-discontinuous or non-homogeneous, an explicit boundary loss with n_{bc} collocation points per edge is employed instead. Similarly, the number of PDE collocation points N_{pde} and the boundary exclusion threshold d_{min} are selected on a per-problem basis to balance physics sampling density against computational cost; representative values are given in Section 5.

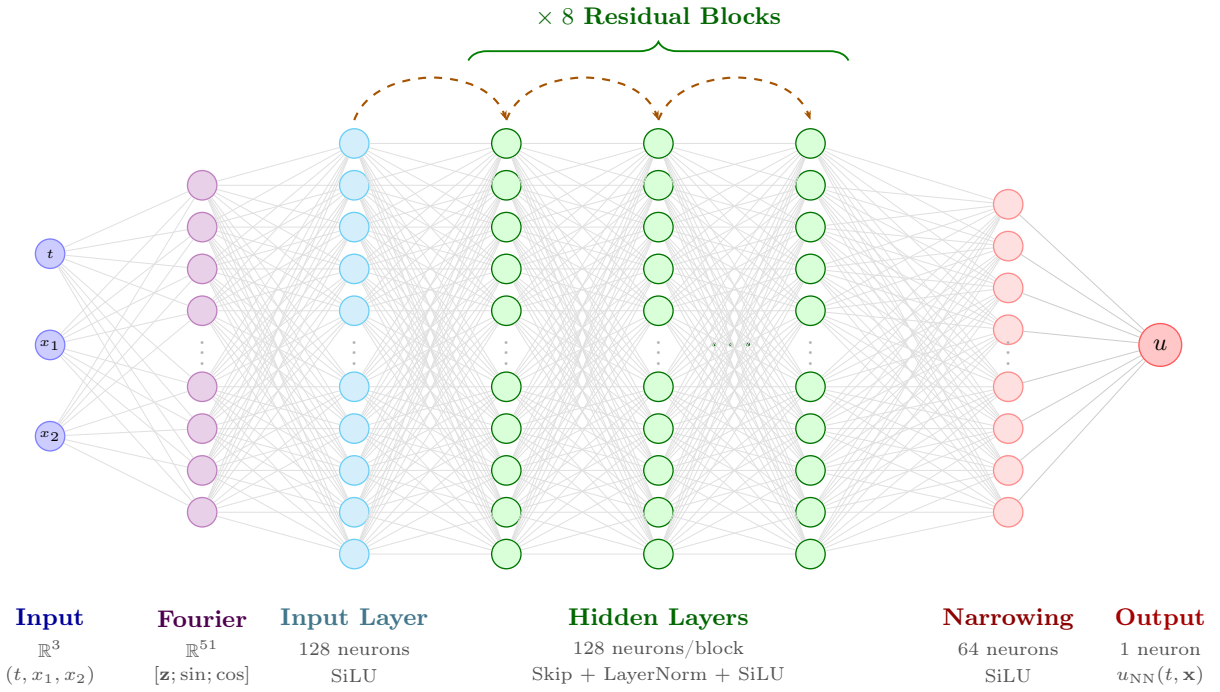


Figure 2: Schematic of the PASSC neural network architecture (shown for $n_h = 128$, $n_r = 8$, $n_F = 24$, $n_{sd} = 2$). The spatiotemporal input $\mathbf{z} = (t, x_1, x_2) \in \mathbb{R}^3$ is mapped through a random Fourier feature embedding to $\varphi(\mathbf{z}) \in \mathbb{R}^{51}$, projected to a hidden dimension of 128 via the input layer with SiLU activation, and then processed by 8 residual blocks—each comprising two fully connected layers, a skip (residual) connection, and layer normalization. A narrowing layer ($128 \rightarrow 64$) followed by a single output neuron produces the predicted solution $u_{NN}(t, \mathbf{x})$.

4. Further Computational Details

This section describes the computational framework developed to implement and validate the proposed hybrid methodology. It covers the scientific computing environment, spatial discretization schemes, mesh generation strategies, and solution techniques for the resulting linear and nonlinear algebraic systems, as well as the PyTorch environment and CUDA technology.

4.1. Scientific Computing Environment: *FEniCS*

FEniCS [32, 33, 73] is an open-source scientific computing platform specifically designed for the numerical solution of partial differential equations (PDEs). It provides a robust and flexible infrastructure for developing FEM-based solvers and has been selected as the primary computational environment in this study. Owing to its versatility, **FEniCS** offers an ideal framework for implementing both stabilized finite element methods and PINNs. Its C++ and/or Python-based interface allows for concise expression of complex mathematical models and seamless integration with a wide array of machine learning libraries—an essential capability for optimizing stabilization and shock-capturing parameters within a unified environment. Moreover, **FEniCS** is compatible with high-performance computing (HPC) systems, supporting parallel computations that are essential for solving large-scale and computationally intensive problems. This scalability is particularly advantageous when addressing time-dependent and three-dimensional PDEs, contributing to the robustness and flexibility of the numerical investigations in this study. Here, **FEniCS** (2019.2.0.64.dev0) serves as the core computational platform for implementing and validating the standard and stabilized finite element formulations and their integration with PINNs. The SUPG stabilization and $YZ\beta$ shock-capturing techniques are developed within the **FEniCS** environment and combined with machine learning strategies.

FEniCS also has a newer version called **FEniCSx** [74], which offers enhanced performance through modern C++ architecture, improved scalability, and better integration with contemporary scientific computing ecosystems. For more details on both the legacy and new versions of the **FEniCS** project, interested readers can refer to the project webpage <https://fenicsproject.org/>.

4.2. *PyTorch* and *CUDA*

PyTorch [75] is utilized in this study as the core deep learning framework for implementing PINNs. Its dynamic computation graph, user-friendly interface, and strong support for GPU acceleration via **CUDA** (Compute Unified Device Architecture) make it a suitable choice for training neural networks in complex, physics-driven settings. **PyTorch** enables the automatic differentiation of loss functions that include not only standard PDE residuals but also contributions from SUPG stabilization and $YZ\beta$ shock-capturing terms, as introduced in Section 3. This capability is essential for efficiently computing gradients during backpropagation and updating model parameters in a stable manner. In order to enhance computational performance, particularly for high-resolution spatiotemporal problems and deep network architectures, all **PyTorch**-based PINN models are trained on **NVIDIA** GPUs using **CUDA**. The **CUDA** backend allows substantial speedup in both forward passes and gradient computations, which significantly reduces the total training time.

The integration between **PyTorch** and **FEniCS** is facilitated by the Python ecosystem, allowing seamless data transfer between the finite element solver and the neural network. In particular, quantities such as element-wise parameters, geometric characteristics, and PDE residuals computed in **FEniCS** are passed as inputs to the **PyTorch** network to enable localized adaptivity during training.

For more details on **PyTorch**, the reader is referred to the official webpage of the project: <https://pytorch.org/>.

4.3. Finite Element Mesh Construction

In this work, 1D and 2D geometries are considered, and finite element meshes are generated to support the numerical simulations. The built-in `mshr` module of `FEniCS` is employed to generate finite element meshes directly within the `Python` environment. This enables rapid mesh generation and seamless integration into the overall simulation workflow.

4.4. Time Integration

The spatially semi-discrete system arising from the stabilized finite element formulation is advanced in time using the backward Euler method. Given the discrete solution $u^{h,n} \in \mathcal{S}_u^h$ at time level t^n , the solution $u^{h,n+1}$ at $t^{n+1} = t^n + \Delta t$ is obtained by solving the following fully discrete variational problem: find $u^{h,n+1} \in \mathcal{S}_u^h$ such that

$$\begin{aligned} & \int_{\Omega} \frac{u^{h,n+1} - u^{h,n}}{\Delta t} w^h d\Omega + \int_{\Omega} (\varepsilon \nabla u^{h,n+1} \cdot \nabla w^h + (\mathbf{b}^{n+1} \cdot \nabla u^{h,n+1}) w^h + c u^{h,n+1} w^h - f^{n+1} w^h) d\Omega \\ & + \sum_{e=1}^{n_{el}} \int_{\Omega^e} \tau_{\text{SUPG}} (\mathbf{b}^{n+1} \cdot \nabla w^h) \mathcal{R}^h(u^{h,n+1}) d\Omega + \sum_{e=1}^{n_{el}} \int_{\Omega^e} \nu_{\text{SHOC}} \nabla w^h \cdot \nabla u^{h,n+1} d\Omega = 0, \end{aligned} \quad (50)$$

for all $w^h \in \mathcal{V}_u^h$, where $\mathbf{b}^{n+1} = \mathbf{b}(t^{n+1}, \mathbf{x})$ and $f^{n+1} = f(t^{n+1}, \mathbf{x})$ denote the convection velocity and source term evaluated at the implicit time level, respectively. For nonlinear problems in which the convection velocity depends on the solution itself (e.g., Burgers' equation with $\mathbf{b} = (u, u)^\top$), the implicit dependence $\mathbf{b}^{n+1} = \mathbf{b}(u^{h,n+1})$ is resolved through the Newton–Raphson linearization described in the next section. The strong-form residual at time level $n + 1$ is defined as

$$\mathcal{R}^h(u^{h,n+1}) = \frac{u^{h,n+1} - u^{h,n}}{\Delta t} - \varepsilon \Delta u^{h,n+1} + \mathbf{b}^{n+1} \cdot \nabla u^{h,n+1} + c u^{h,n+1} - f^{n+1}. \quad (51)$$

4.5. Numerical Solution of Linear and Nonlinear Systems of Algebraic Equations

The stabilized formulation of the governing equations, as described in Eq. (11), leads to a system of nonlinear equations. These nonlinear systems are solved using the Newton–Raphson (N–R) method, which provides a robust framework for linearizing and iteratively solving nonlinear PDEs. At each nonlinear iteration, the resulting linear systems are addressed using different strategies depending on the problem size and computational setting. For small-scale problems, direct solvers based on LU (lower-upper) decomposition are employed due to their efficiency and ease of implementation. In serial computations, the built-in `PETSc` (Portable, Extensible Toolkit for Scientific Computation) [76] support in `FEniCS` is used to access a wide variety of linear algebra routines. In cases where direct solvers become infeasible due to memory constraints or extreme problem size, iterative solvers such as `GMRES` (Generalized Minimal Residual Method) [77] are adopted. `GMRES` is supported by `ILU` (incomplete lower-upper) preconditioning to accelerate convergence in sparse and poorly conditioned systems.

5. Test Computations

This section presents a comprehensive set of numerical examples to evaluate the performance and robustness of the proposed hybrid framework. The test problems are carefully selected to cover a wide range of transient

scenarios, assessing the accuracy, stability, and adaptive capabilities of the method, particularly in the presence of steep gradients, discontinuities, and shock-like features. Where applicable, comparisons with classical methods are provided to highlight the advantages of the developed approach. All computations are performed on a system equipped with an Intel Core Ultra 9 275HX processor (24 cores) and an NVIDIA GeForce RTX 5070 GPU (8 GB VRAM), running Ubuntu 24.04.3 LTS with CUDA Toolkit 13.0.

5.1. Example 1.

As the first test example, consider the following 1D parabolic initial-boundary value problem [78]:

$$\begin{cases} u_t - \varepsilon u_{xx} + (1 + x(1 - x))u_x = f(t, x), & (t, x) \in (0, 1] \times (0, 1), \\ u(0, x) = u_0(x), & 0 < x < 1, \\ u(t, 0) = 0, \quad u(t, 1) = 0, & 0 \leq t \leq 1, \end{cases} \quad (52)$$

where the initial data $u_0(x)$ and the source function $f(t, x)$ are chosen to fit the exact solution

$$u(t, x) = \exp(-t) \left(C_1 + C_2 x - \exp\left(\frac{x-1}{\varepsilon}\right) \right), \quad (53)$$

with $C_1 = \exp(-1/\varepsilon)$ and $C_2 = 1 - \exp(-1/\varepsilon)$.

Remark 19. In *Example 1*, since the problem is one-dimensional, we simplify the notation by using x instead of x_1 to denote the spatial coordinate.

For the finite element setting, we choose $\varepsilon = 10^{-4}$, $n_{\text{el}} = 200$, $\Delta t = 0.0025$ ($N_t = 400$), and $Y = 0.1$. The PINN architecture employs $n_h = 128$, $n_r = 8$, $n_F = 24$, and $\sigma = 4.0$. Training uses the last $K_s = 10$ temporal snapshots near the terminal time $t_f = 1.0$, with a batch size 256, an initial learning rate $\alpha = 10^{-4}$, and a gradient clipping threshold $g_{\text{max}} = 0.3$. The PDE residual is evaluated at $N_{\text{pde}} = 512$ randomly sampled interior collocation points every third mini-batch to reduce computational cost. The phase boundaries and adaptive weights are presented in Table 1.

Table 1: Phase boundaries and adaptive weights used for solving *Example 1*.

| Phase | Epochs | w_{data} | w_{pde} | w_{bc} |
|-------|-----------|-------------------|------------------|-----------------|
| I | 0–1499 | 1.0 | 0.5 | 0.1 |
| II | 1500–2999 | 0.8 | 0.95 | 0.1 |
| III | 3000–4999 | 0.35 | 5.0 | 0.1 |

Figure 3 presents the numerical solutions at the terminal time $t_f = 1$ for $\varepsilon = 10^{-4}$. On the global scale (Figure 3a), all three numerical approximations—SUPG, SUPG-YZ β , and the hybrid PINN—are visually indistinguishable from the analytical solution throughout the interior of the domain, where the solution varies smoothly and nearly linearly. The critical differences emerge in the boundary layer region near $x = 1$, which is magnified in Figure 3b. There, the SUPG solution exhibits pronounced node-to-node oscillations that extend

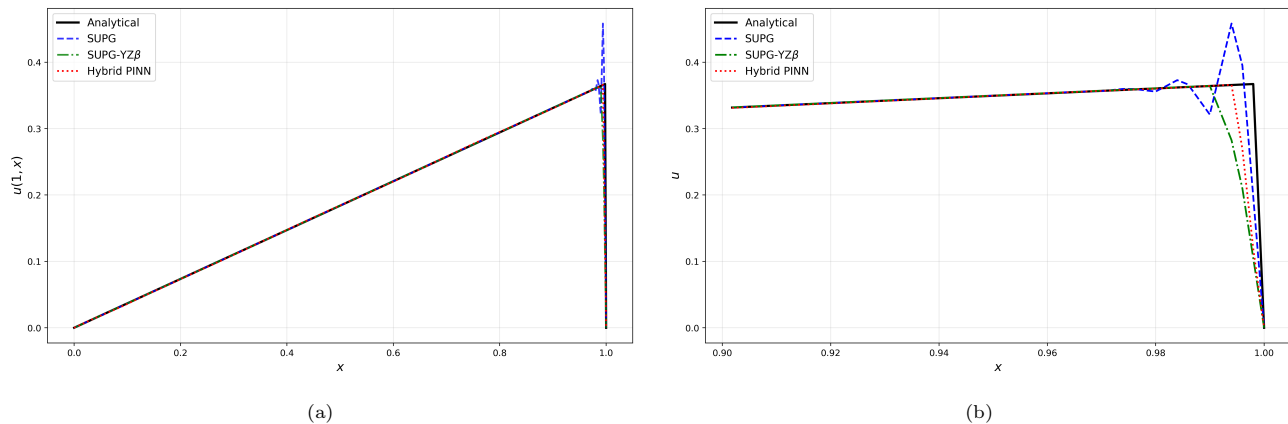


Figure 3: Comparison of the numerical solutions obtained by SUPG, SUPG-YZ β , and the hybrid PINN with the analytical solution for *Example 1* with $\varepsilon = 10^{-4}$: (a) entire domain and (b) zoom in the boundary layer region near $x = 1$.

into the interior, a well-known artifact of insufficient crosswind dissipation in the presence of exponentially steep gradients of width $\mathcal{O}(\varepsilon)$. The addition of the YZ β shock-capturing operator suppresses the oscillatory overshoot, yielding a monotone profile; however, the SUPG-YZ β solution introduces a slight smearing of the layer, as the isotropic artificial diffusion broadens the transition region beyond its analytical extent. The hybrid PINN correction recovers a sharper and more accurate representation of the boundary layer, closely tracking the analytical profile. This improvement is attributable to the physics-informed refinement: the network, having learned the global solution structure from the SUPG-YZ β reference data, enforces the governing PDE residual via automatic differentiation, which acts as a regularizer that sharpens the layer without reintroducing spurious oscillations.

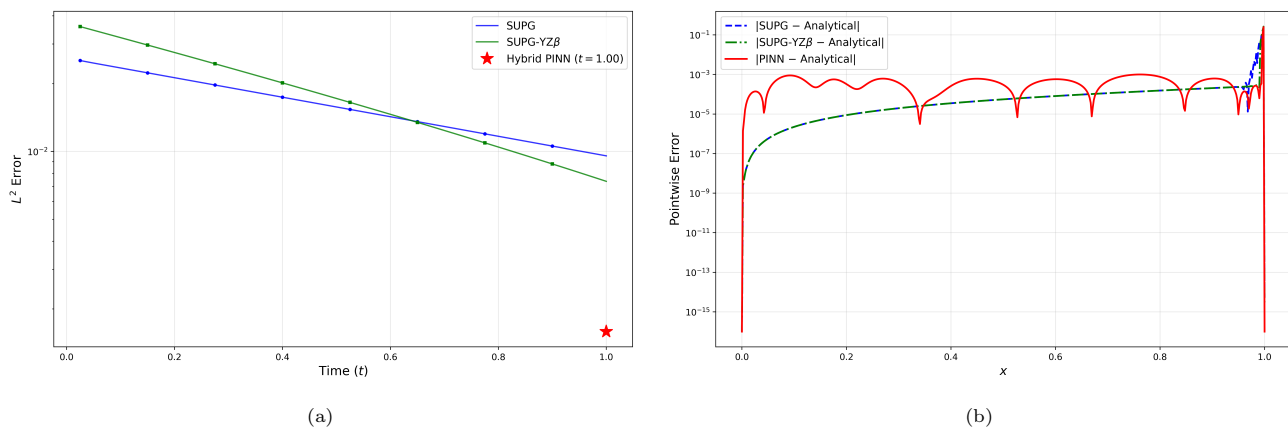


Figure 4: Error analysis for *Example 1* with $\varepsilon = 10^{-4}$: (a) evolution of the L^2 error over the time interval $[0, 1]$ for SUPG and SUPG-YZ β , with the hybrid PINN error at the terminal time $t_f = 1$ indicated by the star marker; (b) pointwise absolute error at $t_f = 1$ across the spatial domain.

The error analysis in Figure 4 provides a quantitative assessment of the three methods. Figure 4a displays the temporal evolution of the L^2 error norm. Both FEM solvers exhibit a monotonically decreasing error over the simulation interval, with the SUPG-YZ β formulation consistently outperforming the SUPG-only discretization

owing to the additional shock-capturing dissipation. Notably, the hybrid PINN correction at the terminal time $t_f = 1$ (red star) achieves an L^2 error approximately two orders of magnitude below the SUPG- $YZ\beta$ solution, demonstrating the substantial accuracy gain afforded by the physics-informed post-processing step. The spatial distribution of the pointwise error at $t_f = 1$, shown in Figure 4b, reveals further structural differences among the methods. The SUPG solution maintains an error of $\mathcal{O}(10^{-5})$ in the smooth interior but exhibits a sharp spike near $x = 1$, where the boundary layer oscillations produce errors exceeding $\mathcal{O}(10^{-1})$. The SUPG- $YZ\beta$ solution distributes the error more uniformly at $\mathcal{O}(10^{-5})$ across the domain, effectively eliminating the boundary layer spike at the cost of slightly elevated error in the smooth region due to the additional artificial diffusion. The hybrid PINN error profile, by contrast, displays a qualitatively different character: the pointwise error oscillates between $\mathcal{O}(10^{-7})$ and $\mathcal{O}(10^{-3})$, with several localized dips approaching machine precision. This non-uniform error distribution reflects the spectral approximation properties of the Fourier feature embedding, which allocates representational capacity across multiple frequency scales rather than distributing the error uniformly.

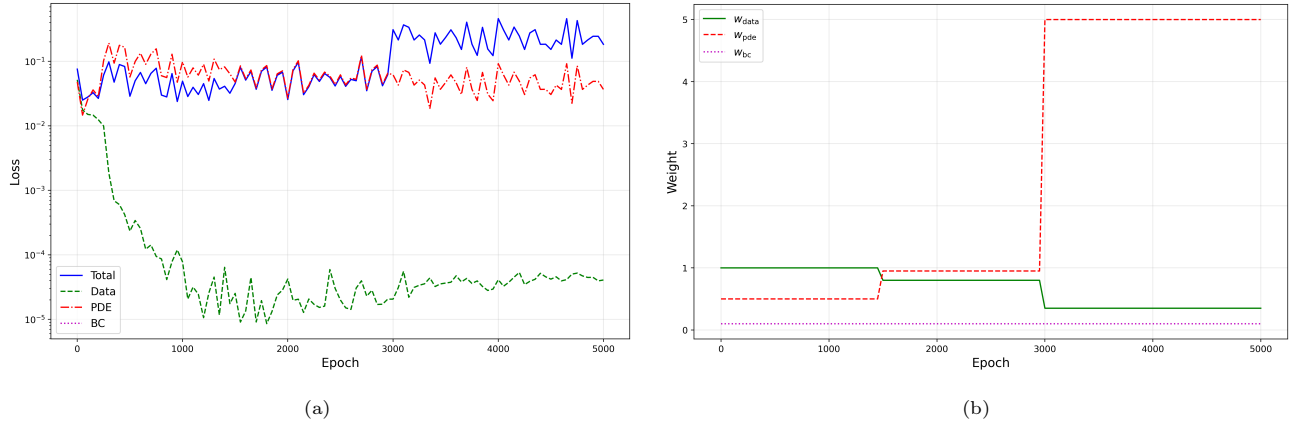


Figure 5: Training diagnostics for *Example 1* with $\varepsilon = 10^{-4}$: (a) evolution of the individual loss components (total, data, PDE, and BC) over 5000 training epochs on a logarithmic scale; (b) adaptive weight schedule w_{data} , w_{pde} , and w_{bc} governing the three-phase training strategy.

The training dynamics of the hybrid PINN for *Example 1* are illustrated in Figure 5. The loss evolution in Figure 5a reveals the distinct behavior of each component across the three training phases. During Phase I (epochs 0–1499), where data fidelity dominates with $w_{\text{data}} = 1.0$, the data loss decreases rapidly from $\mathcal{O}(10^{-2})$ to $\mathcal{O}(10^{-4})$, indicating that the network successfully learns the global solution structure from the SUPG- $YZ\beta$ reference snapshots. The PDE loss remains at $\mathcal{O}(10^{-1})$ during this phase, as the physics constraint receives only moderate weight ($w_{\text{pde}} = 0.5$). The transition to Phase II (epochs 1500–2999) slightly increases the PDE influence to $w_{\text{pde}} = 0.95$ while reducing the data weight to $w_{\text{data}} = 0.8$, producing a gradual shift toward physics-driven learning. In Phase III (epochs 3000–4999), the PDE weight rises sharply to $w_{\text{pde}} = 5.0$ while the data weight drops to $w_{\text{data}} = 0.35$, as shown in the weight schedule of Figure 5b. The total loss increases accordingly, reflecting the now-dominant PDE residual contribution; however, the data loss continues to decrease steadily, confirming that physics-informed refinement does not compromise the learned solution fidelity. The boundary condition loss remains identically zero throughout training, as the lift-based distance function $d(x) = x(1 - x)$ enforces

homogeneous Dirichlet conditions exactly by construction (see Remark 15), rendering the weight $w_{bc} = 0.1$ inconsequential.

5.2. Example 2.

Consider the following 2D convection-diffusion-reaction equation (hump changing its height) [17, 79]:

$$\begin{cases} \frac{\partial u}{\partial t} - \varepsilon \Delta u + \mathbf{b} \cdot \nabla u + cu = f, & (x_1, x_2) \in \Omega, \quad t \in (0, t_f], \\ u(0, x_1, x_2) = u_0(x_1, x_2), & (x_1, x_2) \in \Omega, \\ u = 0, & (x_1, x_2) \in \partial\Omega, \quad t \in [0, t_f], \end{cases} \quad (54)$$

where $\Omega = (0, 1)^2$, $t_f = 0.5$, $\varepsilon = 10^{-6}$, $\mathbf{b} = (2, 3)^\top$, and $c = 1$. The forcing term f , the initial condition u_0 , and the boundary conditions are chosen such that the exact solution

$$u(t, x_1, x_2) = 16 \sin(\pi t) x_1(1 - x_1) x_2(1 - x_2) \left[\frac{1}{2} + \frac{\arctan(2\varepsilon^{-1/2} (0.25^2 - (x_1 - 0.5)^2 - (x_2 - 0.5)^2))}{\pi} \right] \quad (55)$$

is satisfied.

This problem was also considered in [17, 79]. In [17], the authors compare several shock-capturing mechanisms and show that they all fail for this particular type of problem by producing spurious stripes around the hump.

For the finite element setting, we choose $\varepsilon = 10^{-6}$, $n_{el} = 8,192$ (structured triangulation of a 64×64 grid), $\Delta t = 0.0025$ ($N_t = 200$), and $Y = 0.7$. The PINN architecture employs $n_h = 128$, $n_r = 8$, $n_F = 24$, and $\sigma = 4.0$. Training uses the last $K_s = 5$ temporal snapshots near $t_f = 0.5$, with batch size 16000, initial learning rate $\alpha = 8 \times 10^{-5} \sqrt{N_{batch}/256} \approx 6.3 \times 10^{-4}$ (square-root scaling), and gradient clipping threshold $g_{max} = 1.0$. The PDE residual is evaluated at $N_{pde} = 256$ randomly sampled interior collocation points per mini-batch. The phase boundaries and adaptive weights are reported in Table 2.

Table 2: Phase boundaries and adaptive weights used for solving *Example 2*.

| Phase | Epochs | w_{data} | w_{pde} | w_{bc} |
|-------|-----------|------------|-----------|----------|
| I | 0–999 | 1.0 | 0.05 | 0.01 |
| II | 1000–1499 | 0.5 | 0.1 | 0.05 |
| III | 1500–4999 | 0.1 | 0.5 | 0.1 |

Figure 6 displays the three-dimensional solution profiles at $t = 0.5$ for *Example 2*. The analytical solution (Figure 6a) features a smooth, compactly supported hump centered at $(x_1, x_2) = (0.5, 0.5)$ whose amplitude is modulated by the factor $16 \sin(\pi t)$, reaching its peak value at the selected time level. The hump possesses extremely steep flanks governed by the arctangent layer of width $\mathcal{O}(\sqrt{\varepsilon}) = \mathcal{O}(10^{-3})$, making this a particularly challenging test case. As noted in [17], all classical shock-capturing mechanisms fail for this problem type, and the SUPG-YZ β approximation in Figure 6b confirms this observation: pronounced spurious stripes appear around the base and flanks of the hump, together with localized oscillations in the flat region where the solution should

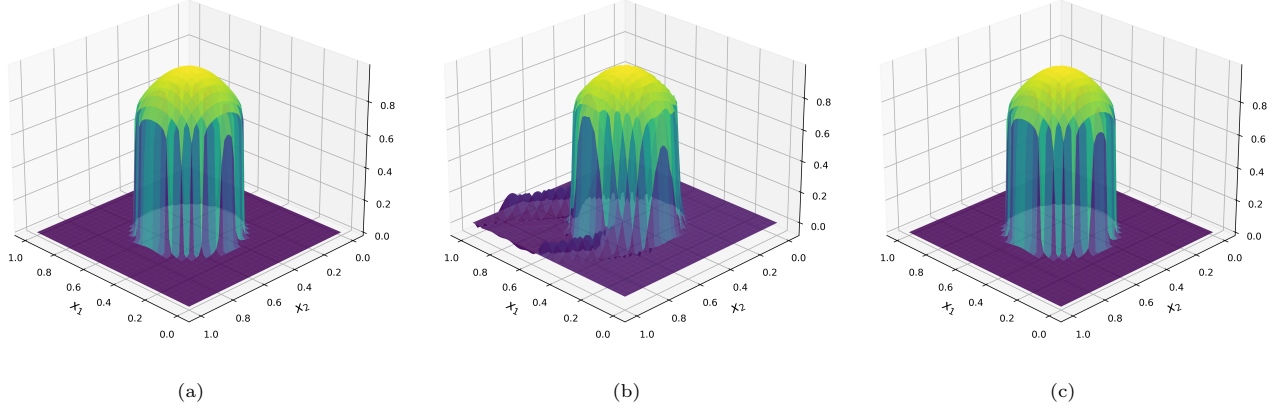


Figure 6: Three-dimensional surface plots of the solution to *Example 2* at $t = 0.5$ with $\varepsilon = 10^{-6}$: (a) analytical solution; (b) SUPG-YZ β finite element approximation; (c) hybrid PINN correction.

vanish identically. These artifacts arise because the isotropic shock-capturing diffusion interacts adversely with the circular symmetry of the internal layer, generating crosswind distortions that propagate along the convection direction $\mathbf{b} = (2, 3)^\top$. The hybrid PINN correction (Figure 6c) substantially eliminates these spurious features, recovering a surface profile that closely matches the analytical solution. The hump shape, peak amplitude, and steep flanks are faithfully reproduced, while the oscillatory stripes visible in the FEM approximation are effectively suppressed. This result demonstrates the capacity of the physics-informed post-processing to correct structural artifacts that persist even after stabilization and shock-capturing have been applied.

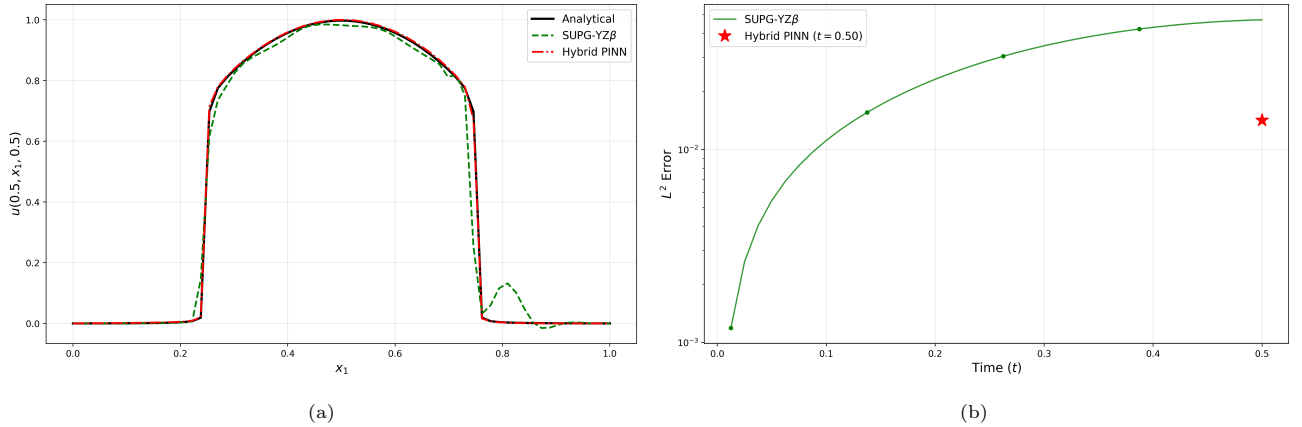


Figure 7: Quantitative comparison for *Example 2* with $\varepsilon = 10^{-6}$: (a) cross-sectional profiles along $x_2 = 0.5$ at $t = 0.5$, comparing the analytical solution, SUPG-YZ β , and hybrid PINN; (b) evolution of the L^2 error over the time interval $[0, 0.5]$ for SUPG-YZ β , with the hybrid PINN error at the terminal time indicated by the star marker.

A more quantitative assessment is provided in Figure 7. The cross-sectional profile along $x_2 = 0.5$ at $t = 0.5$ (Figure 7a) reveals the detailed structure of the internal layer. The analytical solution displays a sharp, symmetric hump with a flat plateau near unity and steep flanks transitioning to zero over a distance of $\mathcal{O}(\sqrt{\varepsilon})$. The SUPG-YZ β approximation captures the overall shape but exhibits two characteristic deficiencies: the steep

flanks are smeared relative to the exact profile, and a spurious secondary bump of amplitude ~ 0.13 appears near $x_1 \approx 0.8$, corresponding to the stripe artifact visible in the three-dimensional view of Figure 6b. The hybrid PINN correction eliminates this spurious feature entirely and recovers steeper flanks that track the analytical profile more faithfully, although a slight undershoot is observed at the downstream transition near $x_1 \approx 0.75$. The temporal evolution of the L^2 error norm in Figure 7b shows a monotonically increasing trend for the SUPG- $\text{YZ}\beta$ solution, rising from $\mathcal{O}(10^{-3})$ at early times to $\mathcal{O}(10^{-2})$ at $t = 0.5$. This growth reflects the progressive accumulation of the stripe artifacts as the hump amplitude increases with $\sin(\pi t)$. The hybrid PINN error at the terminal time (red star) lies below the SUPG- $\text{YZ}\beta$ error curve, confirming that the physics-informed correction yields a measurable improvement in global accuracy despite operating only on the final temporal snapshots.

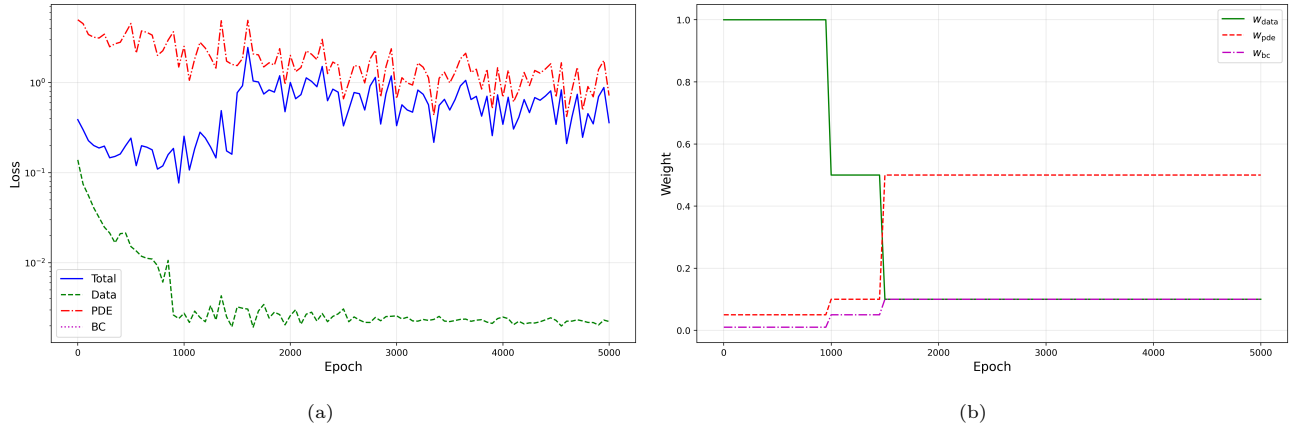


Figure 8: Training diagnostics for *Example 2* with $\varepsilon = 10^{-6}$: (a) evolution of the individual loss components (total, data, PDE, and BC) over 5000 training epochs on a logarithmic scale; (b) adaptive weight schedule w_{data} , w_{pde} , and w_{bc} governing the three-phase training strategy.

The training diagnostics for *Example 2* are presented in Figure 8. Compared with the 1D case of *Example 1* (see Figure 5), the loss landscape exhibits markedly different behavior, reflecting the increased complexity of the two-dimensional hump problem. As shown in Figure 8a, the data loss decreases steadily from $\mathcal{O}(10^{-1})$ to $\mathcal{O}(10^{-2})$ during Phase I (epochs 0–999), where the data weight dominates with $w_{\text{data}} = 1.0$. However, the PDE loss remains persistently elevated at $\mathcal{O}(1)$ – $\mathcal{O}(10)$ throughout training, substantially higher than in *Example 1*. This elevated residual is expected: the steep internal layer of width $\mathcal{O}(\sqrt{\varepsilon}) = \mathcal{O}(10^{-3})$ generates large pointwise PDE residuals that resist minimization, particularly in the transition regions around the hump flanks.

The weight schedule in Figure 8b reveals the deliberately conservative physics enforcement adopted for this problem. Upon transitioning from Phase I to Phase II at epoch 1000, the data weight drops from 1.0 to 0.5 while the PDE weight increases modestly from 0.05 to 0.1. In Phase III (epochs 1500–4999), the weights stabilize at $w_{\text{data}} = 0.1$ and $w_{\text{pde}} = 0.5$ —notably milder than the aggressive physics-dominant configuration used in *Example 1* ($w_{\text{pde}} = 5.0$). This restraint is deliberate: excessive PDE weight enforcement for the hump problem risks reintroducing the spurious stripe artifacts that the PINN correction is designed to eliminate. The boundary condition loss remains at low levels throughout training, consistent with the lift-based enforcement via the

distance function $d(\mathbf{x}) = x_1(1 - x_1)x_2(1 - x_2)$.

5.3. Example 3.

Consider the following 2D convection-diffusion-reaction equation (traveling wave) [79]:

$$\begin{cases} \frac{\partial u}{\partial t} - \varepsilon \Delta u + \mathbf{b} \cdot \nabla u + cu = f, & (x_1, x_2) \in \Omega, \quad t \in (0, t_f], \\ u = 0, & (x_1, x_2) \in \partial\Omega, \quad t \in [0, t_f], \\ u(0, x_1, x_2) = u_0(x_1, x_2), & (x_1, x_2) \in \Omega, \end{cases} \quad (56)$$

where $\Omega = (0, 1)^2$, $t_f = 1$, $\varepsilon = 10^{-8}$, $\mathbf{b} = (\cos(\pi/3), \sin(\pi/3))^\top$, and $c = 1$. The forcing term f , the initial condition u_0 , and the boundary conditions are chosen such that the exact solution

$$u(t, x_1, x_2) = 0.5 \sin(\pi x_1) \sin(\pi x_2) \left[\tanh\left(\frac{x_1 + x_2 - t - 0.5}{\sqrt{\varepsilon}}\right) + 1 \right] \quad (57)$$

is satisfied. The solution possesses a moving internal layer of width $\mathcal{O}(\sqrt{\varepsilon})$.

For the finite element setting, we set $n_{\text{el}} = 8192$ (structured triangulation of a 64×64 grid), $\Delta t = 0.001$ ($N_t = 1000$), and $Y = 0.25$. The moving internal layer of width $\mathcal{O}(\sqrt{\varepsilon}) = \mathcal{O}(10^{-4})$ necessitates a finer temporal resolution compared to *Example 2* to accurately track the propagating front. The PINN architecture employs a smaller network with $n_h = 96$, $n_r = 6$, $n_F = 16$, and $\sigma = 4.0$, reflecting the lower-dimensional structure of the traveling wave solution compared to the hump problem. Training uses the last $K_s = 5$ temporal snapshots near $t_f = 1.0$, with batch size 16000, initial learning rate $\alpha \approx 6.3 \times 10^{-4}$ (square-root scaling), and gradient clipping threshold $g_{\text{max}} = 1.0$. The PDE residual is evaluated at $N_{\text{pde}} = 384$ randomly sampled interior collocation points per mini-batch. Since the network architecture incorporates the lift-based distance function $d(\mathbf{x}) = x_1(1 - x_1)x_2(1 - x_2)$, the boundary loss is omitted entirely ($w_{\text{bc}} = 0$) throughout all training phases, as Dirichlet conditions are satisfied exactly by construction (see Remark 15). The phase boundaries and adaptive weights are reported in Table 3.

Table 3: Phase boundaries and adaptive weights used for solving *Example 3*.

| Phase | Epochs | w_{data} | w_{pde} | w_{bc} |
|-------|-----------|-------------------|------------------|-----------------|
| I | 0–999 | 1.0 | 0.05 | 0.0 |
| II | 1000–1499 | 0.5 | 0.1 | 0.0 |
| III | 1500–4999 | 0.1 | 0.5 | 0.0 |

Figure 9 presents the three-dimensional solution profiles at the terminal time $t_f = 1$ for *Example 3*. The analytical solution (Figure 9a) features a localized traveling wave peak resulting from the interaction of the sinusoidal envelope $0.5 \sin(\pi x_1) \sin(\pi x_2)$ with the internal layer governed by the hyperbolic tangent profile of width $\mathcal{O}(\sqrt{\varepsilon}) = \mathcal{O}(10^{-4})$. This extremely thin moving front poses a severe challenge for all numerical methods. The SUPG solution (Figure 9b) fails dramatically: in the absence of shock-capturing, the unstabilized crosswind

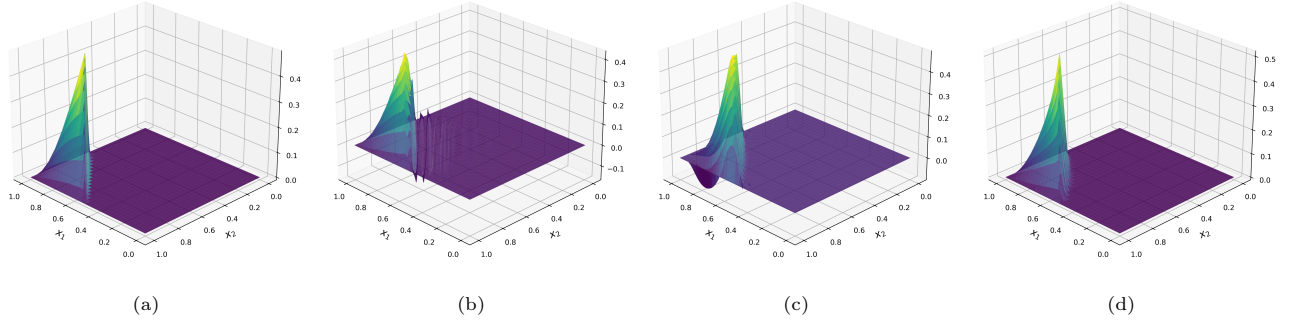


Figure 9: Three-dimensional surface plots of the solution to *Example 3* at $t_f = 1$ with $\varepsilon = 10^{-8}$: (a) analytical solution; (b) SUPG finite element approximation; (c) SUPG- $\text{YZ}\beta$ finite element approximation; (d) hybrid PINN correction.

diffusion generates pronounced undershoots reaching approximately -0.1 , together with widespread oscillatory artifacts that contaminate the entire domain. The addition of $\text{YZ}\beta$ shock-capturing (Figure 9c) eliminates the negative undershoots and suppresses the global oscillations, yielding a non-negative solution; however, the peak amplitude is visibly attenuated and the layer is broadened by the isotropic artificial diffusion, resulting in a smeared profile that underestimates the true solution magnitude. The hybrid PINN correction (Figure 9d) recovers both the sharp layer structure and the correct peak amplitude, producing a surface profile that closely matches the analytical solution. The peak is well-localized, the surrounding flat region remains free of spurious oscillations, and the transition from the elevated region to the zero plateau is captured with substantially higher fidelity than either FEM approximation. This example highlights the particular strength of the hybrid framework for problems involving extremely thin moving fronts, where even stabilized and shock-captured finite element solutions suffer from excessive numerical diffusion.

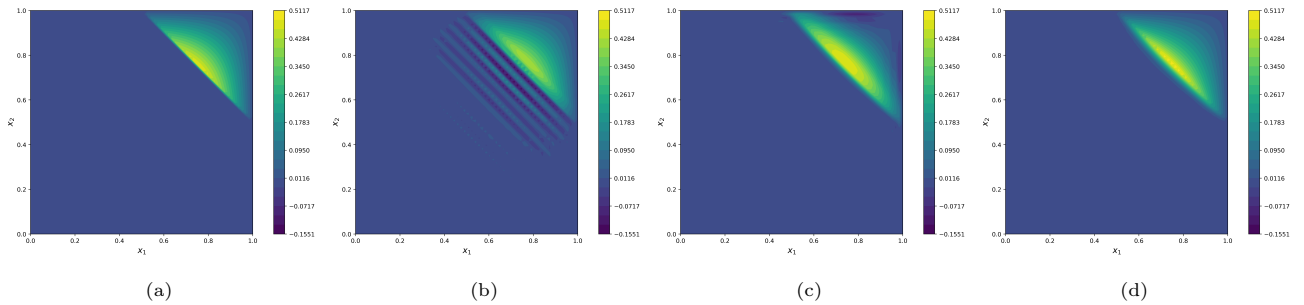


Figure 10: Contour plots of the solution to *Example 3* at $t_f = 1$ with $\varepsilon = 10^{-8}$: (a) analytical solution; (b) SUPG finite element approximation; (c) SUPG- $\text{YZ}\beta$ finite element approximation; (d) hybrid PINN correction. All panels share the same color scale.

The contour plots in Figure 10 provide a top-down view of the same solutions, revealing the spatial structure of the internal layer and its numerical approximations more clearly. The analytical solution (Figure 10a) exhibits a sharp diagonal front oriented along the convection direction $\mathbf{b} = (\cos(\pi/3), \sin(\pi/3))^T$, separating the elevated region near the upper-right corner from the zero-valued exterior. The SUPG contour plot (Figure 10b) exposes the crosswind oscillations as a series of parallel striations aligned perpendicular to the convection direction, extending well into the interior of the domain. These artifacts, which appear as diagonal bands of alternating

positive and negative error, are a hallmark of insufficient crosswind diffusion for convection-dominated problems on structured meshes. The SUPG- $\text{YZ}\beta$ solution (Figure 10c) eliminates the striations entirely, producing a smooth contour field; however, the front is noticeably broadened compared to the analytical reference, and the peak values in the upper-right corner are attenuated. The hybrid PINN contour (Figure 10d) closely reproduces the analytical pattern: the front sharpness is restored, the diagonal orientation is correctly captured, and the solution magnitude in the elevated region matches the reference without the amplitude loss observed in the SUPG- $\text{YZ}\beta$ approximation.

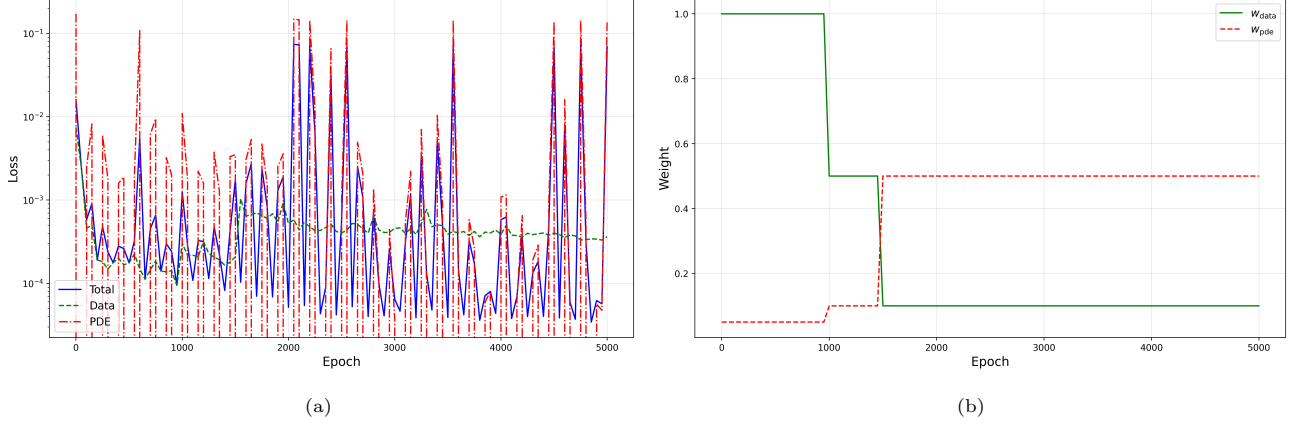


Figure 11: Training diagnostics for *Example 3* with $\varepsilon = 10^{-8}$: (a) evolution of the individual loss components (total, data, and PDE) over 5000 training epochs on a logarithmic scale; (b) adaptive weight schedule w_{data} and w_{pde} governing the three-phase training strategy. The boundary condition weight is omitted ($w_{\text{bc}} = 0$) as Dirichlet conditions are enforced exactly via the distance function.

The training diagnostics for *Example 3* are shown in Figure 11. The loss evolution in Figure 11a reveals a markedly different character compared to the preceding examples. The PDE loss exhibits pronounced intermittent spikes spanning nearly three orders of magnitude, from $\mathcal{O}(10^{-4})$ to $\mathcal{O}(10^{-1})$, persisting throughout all training phases. These bursts arise from the extreme sharpness of the internal layer: when randomly sampled collocation points happen to fall within the transition region of width $\mathcal{O}(\sqrt{\varepsilon}) = \mathcal{O}(10^{-4})$, the PDE residual magnitudes increase dramatically due to the steep gradients, producing isolated high-loss batches. Despite this volatile PDE loss behavior, the data loss decreases steadily from $\mathcal{O}(10^{-3})$ to $\mathcal{O}(10^{-4})$, indicating that the network successfully learns the global solution structure without being destabilized by the sporadic PDE residual spikes. The total loss tracks the PDE contribution during the spike events but returns to the data-driven baseline between them. The weight schedule in Figure 11b follows the same three-phase structure as *Example 2*, with w_{data} decreasing from 1.0 to 0.1 and w_{pde} increasing from 0.05 to 0.5 across the three phases. Notably, the boundary condition weight is set to $w_{\text{bc}} = 0$ throughout training, as the lift-based distance function $d(\mathbf{x}) = x_1(1 - x_1)x_2(1 - x_2)$ enforces homogeneous Dirichlet conditions exactly by construction, rendering a separate BC loss term unnecessary. The conservative PDE weight ceiling of $w_{\text{pde}} = 0.5$ in Phase III—identical to that of *Example 2* and substantially lower than the $w_{\text{pde}} = 5.0$ used in *Example 1*—reflects the deliberate restraint required for problems with extremely thin layers, where aggressive physics enforcement risks amplifying the stochastic residual spikes and destabilizing the training process.

5.4. *Example 4.*

Consider the following 2D uncoupled Burgers' equation [62]:

$$\begin{cases} \frac{\partial u}{\partial t} + u \frac{\partial u}{\partial x_1} + u \frac{\partial u}{\partial x_2} = \frac{1}{\text{Re}} \left(\frac{\partial^2 u}{\partial x_1^2} + \frac{\partial^2 u}{\partial x_2^2} \right), & t \in (0, t_f], \quad (x_1, x_2) \in \Omega, \\ u(t_0, x_1, x_2) = u_0(x_1, x_2), & (x_1, x_2) \in \Omega, \\ u(t, x_1, x_2) = u_D(t, x_1, x_2), & (x_1, x_2) \in \partial\Omega, \quad t \in (0, t_f], \end{cases} \quad (58)$$

where the initial and Dirichlet boundary conditions are prescribed such that the exact solution

$$u(t, x_1, x_2) = \frac{1}{1 + \exp\left(\frac{\text{Re}(x_1 + x_2 - t)}{2}\right)} \quad (59)$$

is satisfied.

For the finite element setting, we set $t_0 = 0$, $t_f = 1.0$, $\text{Re} = 10^4$ ($\varepsilon = 1/\text{Re} = 10^{-4}$), $n_{\text{el}} = 4608$ (structured triangulation of a 48×48 grid), $\Delta t = 0.01$ ($N_t = 100$), and $Y = 0.2$. The PINN architecture employs $n_h = 96$, $n_r = 6$, $n_F = 16$, and $\sigma = 4.0$. Training uses the last $K_s = 5$ temporal snapshots near $t_f = 1.0$, with batch size 5000, initial learning rate $\alpha \approx 3.5 \times 10^{-4}$ (square-root scaling), and gradient clipping threshold $g_{\text{max}} = 1.0$. The PDE residual is evaluated at $N_{\text{pde}} = 256$ randomly sampled interior collocation points per mini-batch.

A distinctive feature of the training strategy for this example is that the data weight is held fixed at $w_{\text{data}} = 1.0$ throughout all training phases, in contrast to the decreasing data weight schedule employed in *Example 1–Example 3*. This design choice is motivated by the nonlinear character of Burgers' equation: since the PDE residual alone does not uniquely determine the solution (the inviscid limit admits infinitely many weak solutions), data fidelity must be maintained at all stages to anchor the network to the correct physical branch. The PDE weight is instead increased gradually across four phases, from $w_{\text{pde}} = 0.01$ in Phase I to $w_{\text{pde}} = 5.0$ in Phase IV, progressively strengthening the physics constraint while preserving data anchoring. The boundary condition weight is set to $w_{\text{bc}} = 0$ throughout, as the network architecture employs a lift function of the form $u_{\text{lift}}(t, \mathbf{x}) = (1 + \exp(\text{Re}(x_1 + x_2 - t)/2))^{-1}$, which satisfies the boundary conditions exactly. The phase boundaries and adaptive weights are reported in Table 4.

Table 4: Phase boundaries and adaptive weights used for solving *Example 4*.

| Phase | Epochs | w_{data} | w_{pde} | w_{bc} |
|-------|-----------|-------------------|------------------|-----------------|
| I | 0–999 | 1.0 | 0.01 | 0.0 |
| II | 1000–1999 | 1.0 | 0.1 | 0.0 |
| III | 2000–3499 | 1.0 | 1.0 | 0.0 |
| IV | 3500–4999 | 1.0 | 5.0 | 0.0 |

Remark 20. For problems with non-homogeneous boundary conditions, the lift function u_{lift} must satisfy the prescribed boundary data but need not coincide with the exact solution. In the present example, the analytical

solution of the two-dimensional Burgers’ equation provides a convenient lift; however, in practice, u_{lift} can be constructed from the boundary data alone—for instance, via harmonic extension or bilinear interpolation of the boundary values into the interior. Alternatively, the SUPG- $\text{YZ}\beta$ finite element solution itself can serve as the lift function, in which case the network correction $d(\mathbf{x})\mathcal{N}_\theta(t, \mathbf{x})$ learns the pointwise discrepancy between the FEM approximation and the true solution.

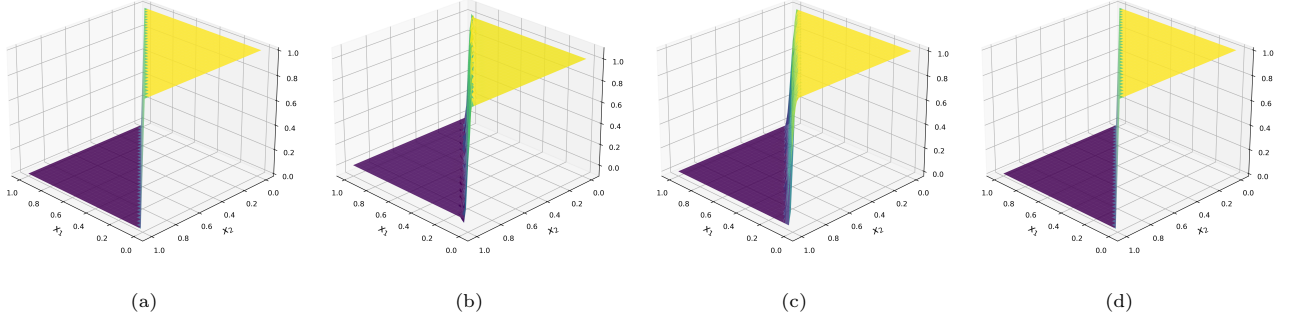


Figure 12: Three-dimensional surface plots of the solution to *Example 4* (two-dimensional Burgers’ equation) at $t_f = 1$ with $\text{Re} = 10^4$: (a) analytical solution; (b) SUPG finite element approximation; (c) SUPG- $\text{YZ}\beta$ finite element approximation; (d) hybrid PINN correction.

Figure 12 displays the three-dimensional solution profiles at $t_f = 1$ for *Example 4*. The analytical solution (Figure 12a) exhibits a sigmoid-type internal layer along the diagonal $x_1 + x_2 = t$, transitioning sharply from $u \approx 1$ in the region $x_1 + x_2 < t$ to $u \approx 0$ in the complement, with the layer width controlled by the Reynolds number as $\mathcal{O}(1/\text{Re}) = \mathcal{O}(10^{-4})$. This problem is particularly demanding because the convection velocity is solution-dependent, causing the front position and steepness to be coupled through the nonlinear self-advection mechanism. The SUPG solution (Figure 12b) captures the overall sigmoid structure and front location but exhibits a visible smearing of the transition region, where the sharp analytical front is replaced by a gradual slope spanning several mesh widths. The SUPG- $\text{YZ}\beta$ approximation (Figure 12c) produces a comparable profile; however, a slight overshoot is discernible at the upper plateau near the front, indicating that the shock-capturing operator does not fully suppress the Gibbs-like oscillations for this nonlinear problem. The hybrid PINN correction (Figure 12d) recovers a steeper front that more closely matches the analytical solution, with the transition region visibly sharper than in either FEM approximation. The improvement is most pronounced along the diagonal, where the self-sharpening mechanism of Burgers’ equation concentrates the solution gradient into an increasingly narrow band that the finite element mesh cannot fully resolve but the neural network, operating in the continuous spatiotemporal domain, can approximate with higher fidelity.

The contour plots in Figure 13 provide a top-down view that more clearly exposes the internal layer structure and the differences among the four solutions. The analytical solution (Figure 13a) displays a sharp diagonal front along $x_1 + x_2 = 1$, with the transition from $u \approx 1$ (yellow, upper-left) to $u \approx 0$ (purple, lower-right) occurring over a distance of $\mathcal{O}(1/\text{Re}) = \mathcal{O}(10^{-4})$. The contour lines are nearly straight and parallel, reflecting the planar symmetry of the exact sigmoid solution along the characteristic direction. The SUPG contour (Figure 13b)

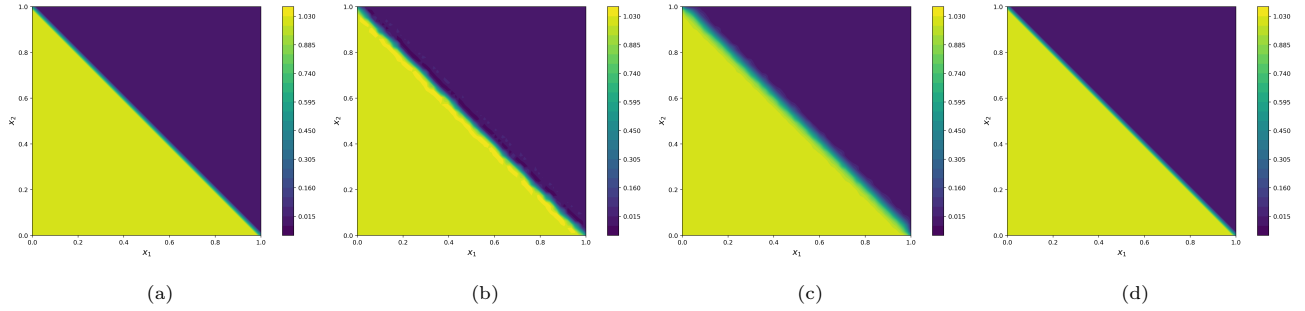


Figure 13: Contour plots of the solution to *Example 4* (two-dimensional Burgers' equation) at $t_f = 1$ with $\text{Re} = 10^4$: (a) analytical solution; (b) SUPG finite element approximation; (c) SUPG- $\text{YZ}\beta$ finite element approximation; (d) hybrid PINN correction. All panels share the same color scale.

reproduces the correct front location and orientation but exhibits a noticeably wider transition band: the green intermediate contours span several mesh widths, indicating numerical diffusion that smears the layer beyond its analytical extent. The SUPG- $\text{YZ}\beta$ solution (Figure 13c) shows a comparable level of front broadening; however, a subtle asymmetry is visible in the contour spacing near the upper-left corner, suggesting that the isotropic shock-capturing diffusion interacts with the nonlinear self-advection to produce a slightly non-uniform layer profile. The hybrid PINN contour (Figure 13d) recovers a sharper front with a narrower transition band that more closely matches the analytical reference, and the contour lines maintain the parallel, planar structure of the exact solution. The improvement is particularly evident in the width of the green intermediate region, which is visibly thinner in the PINN result than in either FEM approximation.

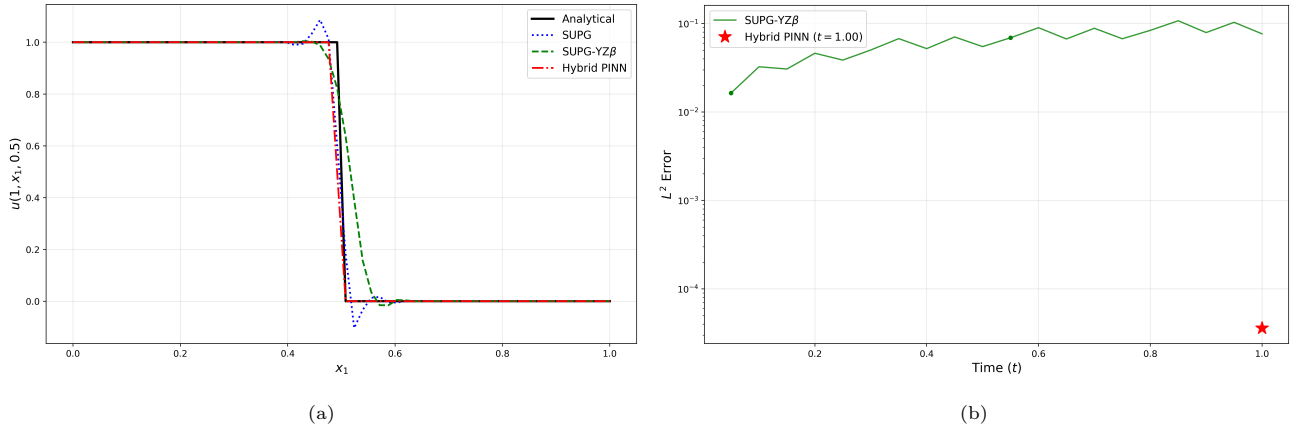


Figure 14: Quantitative comparison for *Example 4* (two-dimensional Burgers' equation) with $\text{Re} = 10^4$: (a) cross-sectional profiles along $x_2 = 0.5$ at $t_f = 1$, comparing the analytical solution, SUPG, SUPG- $\text{YZ}\beta$, and hybrid PINN; (b) evolution of the L^2 error over the time interval $[0, 1]$ for SUPG- $\text{YZ}\beta$, with the hybrid PINN error at the terminal time indicated by the star marker.

The cross-sectional profile along $x_2 = 0.5$ at $t_f = 1$, shown in Figure 14a, provides a one-dimensional slice through the diagonal internal layer at $x_1 + x_2 = 1$, i.e. the front is intersected at $x_1 = 0.5$. The analytical solution exhibits a sharp sigmoid transition from $u = 1$ to $u = 0$ over a distance of $\mathcal{O}(1/\text{Re}) = \mathcal{O}(10^{-4})$. The SUPG solution captures the front location but produces a visible undershoot below zero near $x_1 \approx 0.55$, a characteristic

Gibbs-like artifact of insufficient crosswind stabilization for nonlinear convection. The SUPG- $\text{YZ}\beta$ approximation eliminates the undershoot but introduces substantial smearing: the transition extends over approximately 0.1 units in x_1 , broadening the layer by roughly two orders of magnitude beyond its analytical width. The hybrid PINN correction recovers a significantly steeper front that closely tracks the analytical profile, with neither the undershoot of SUPG nor the excessive smearing of SUPG- $\text{YZ}\beta$. The temporal evolution of the L^2 error in Figure 14b reveals an increasing trend for the SUPG- $\text{YZ}\beta$ solution, growing from $\mathcal{O}(10^{-3})$ at early times to $\mathcal{O}(10^{-1})$ at $t_f = 1$. This monotonic error growth reflects the progressive accumulation of numerical diffusion as the sharp front propagates across the domain: at each time step, the artificial shock-capturing dissipation broadens the layer further, and this diffusive error compounds over the full simulation interval. The hybrid PINN error at the terminal time (red star) lies at approximately $\mathcal{O}(10^{-4})$ —nearly three orders of magnitude below the SUPG- $\text{YZ}\beta$ error—demonstrating the most substantial improvement observed across all examples in this study. This pronounced gain is attributable to the combined effect of the lift-based architecture, which anchors the network to the correct boundary behavior, and the four-phase training strategy with sustained data fidelity ($w_{\text{data}} = 1.0$ throughout), which prevents the nonlinear PDE residual from driving the solution toward spurious branches.

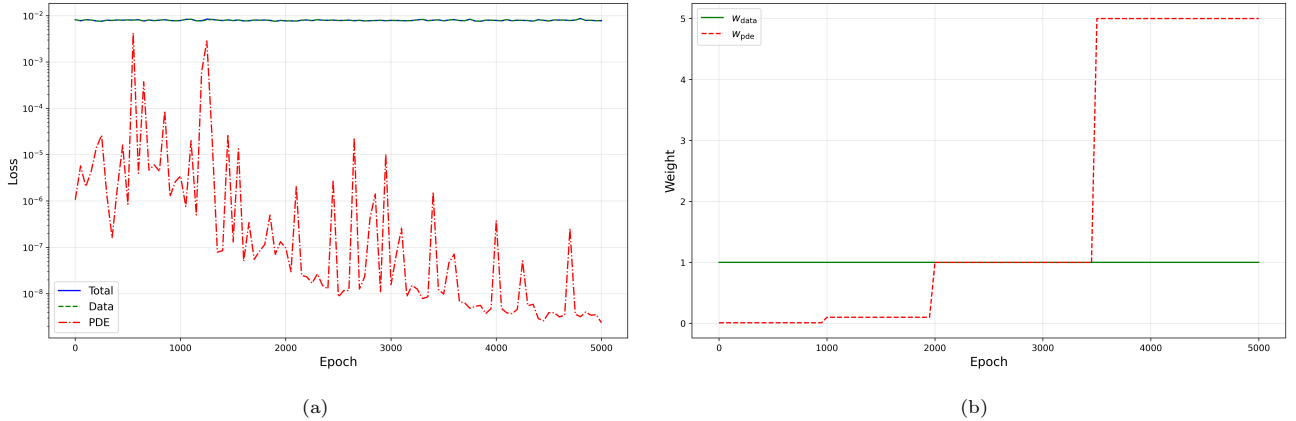


Figure 15: Training diagnostics for *Example 4* (two-dimensional Burgers’ equation) with $\text{Re} = 10^4$: (a) evolution of the individual loss components (total, data, and PDE) over 5000 training epochs on a logarithmic scale; (b) adaptive weight schedule w_{data} and w_{pde} governing the four-phase training strategy. The boundary condition weight is omitted ($w_{\text{bc}} = 0$) as Dirichlet conditions are enforced exactly via the lift function.

The training diagnostics for *Example 4* are presented in Figure 15 and reveal a qualitatively distinct pattern compared to all preceding examples. As shown in Figure 15a, the total and data losses are nearly indistinguishable throughout training, both remaining at a plateau of approximately $\mathcal{O}(10^{-2})$. This behavior is a direct consequence of the lift-based architecture: since the lift function u_{lift} already satisfies the boundary conditions exactly, the network correction $d(\mathbf{x})\mathcal{N}_\theta$ learns a relatively small perturbation, and the data loss—which measures the discrepancy between the network output and the SUPG- $\text{YZ}\beta$ reference—stabilizes at the level of the intrinsic FEM discretization error. The PDE loss exhibits a dramatically different scale, spanning $\mathcal{O}(10^{-8})$ to $\mathcal{O}(10^{-3})$ with intermittent spikes that decrease in both frequency and amplitude over the course of training. This extremely

low PDE residual—several orders of magnitude below the values observed in *Example 1–Example 3*—reflects the smoothness of the correction field: the network need only learn a small adjustment to an already accurate lift, and the resulting PDE residual is correspondingly small. The spikes occur when randomly sampled collocation points intersect the thin internal layer at $x_1 + x_2 = t$, where the solution gradients are of $\mathcal{O}(\text{Re})$. The weight schedule in Figure 15b illustrates the four-phase strategy unique to this example. The data weight remains fixed at $w_{\text{data}} = 1.0$ throughout all phases, in contrast to the decreasing schedule used in *Example 1–Example 3*. This design choice, motivated by the non-uniqueness of weak solutions to Burgers’ equation, ensures that the network remains anchored to the physically correct solution branch at all times. The PDE weight increases progressively from $w_{\text{pde}} = 0.01$ in Phase I through $w_{\text{pde}} = 0.1$ and 1.0 in Phases II and III, culminating at $w_{\text{pde}} = 5.0$ in Phase IV (epochs 3500–4999). Despite this aggressive final PDE weight, the total loss remains dominated by the data component because the PDE residual is inherently small, confirming that the physics-informed training refines the solution without competing against the data fidelity objective.

5.5. Example 5.

Consider the following 2D time-dependent advection–diffusion equation with an L-shaped interior layer [69]:

$$\begin{cases} \frac{\partial u}{\partial t} + \mathbf{b} \cdot \nabla u - \nabla \cdot (\varepsilon \nabla u) = 0, & (x_1, x_2) \in \Omega, \quad t \in (0, t_f], \\ u(0, x_1, x_2) = u_0(x_1, x_2), & (x_1, x_2) \in \Omega, \\ u = g(t, x_1, x_2), & (x_1, x_2) \in \Gamma_D, \quad t \in [0, t_f], \end{cases} \quad (60)$$

where $\Omega = (0, 1)^2$ is the unit square, $t_f = 0.25$, and the diffusivity is $\varepsilon = 10^{-8}$. The advection velocity is

$$\mathbf{b} = |\mathbf{b}|(\cos \theta, \sin \theta)^\top = \left(\frac{\sqrt{2}}{2}, \frac{\sqrt{2}}{2} \right)^\top, \quad (61)$$

with a magnitude $\|\mathbf{b}\| = 1$ and an advection angle $\theta = 45^\circ$ relative to the mesh. The initial condition consists of an L-shaped block:

$$u_0(x_1, x_2) = \begin{cases} 1, & \text{if } (x_1, x_2) \in \Omega_L, \\ 0, & \text{otherwise,} \end{cases} \quad (62)$$

where the L-shaped region Ω_L is defined by

$$\Omega_L = \{(x_1, x_2) : 0 \leq x_1 \leq \frac{1}{2}L, 0 \leq x_2 \leq \frac{1}{4}L\} \cup \{(x_1, x_2) : 0 \leq x_1 \leq \frac{1}{4}L, 0 \leq x_2 \leq \frac{1}{2}L\}, \quad (63)$$

with $L = 1$. The Dirichlet boundary conditions are

$$g(t, x_1, x_2) = \begin{cases} 1, & \text{if } x_2 = 0 \text{ and } 0 \leq x_1 \leq \frac{1}{2}L, \\ 1, & \text{if } x_1 = 0 \text{ and } 0 \leq x_2 \leq \frac{1}{2}L, \\ 0, & \text{otherwise on } \partial\Omega. \end{cases} \quad (64)$$

For the finite element setting, we set $n_{\text{el}} = 8192$ (structured triangulation of a 64×64 grid), $\Delta t = 0.001$ ($N_t = 250$), $t_f = 0.25$, and $Y = 0.25$. Since no analytical solution is available for this problem, the assessment is based on qualitative comparison of the solution profiles and quantitative comparison of the L^2 norms between methods. The PINN architecture employs $n_h = 128$, $n_r = 8$, $n_F = 24$, and $\sigma = 4.0$. Training uses the last $K_s = 10$ temporal snapshots near $t_f = 0.25$, with batch size 2048, initial learning rate $\alpha = 3 \times 10^{-4}$, and gradient clipping threshold $g_{\text{max}} = 1.0$. The PDE residual is evaluated at $N_{\text{pde}} = 4096$ randomly sampled interior collocation points per epoch—the largest value among all examples, chosen to adequately resolve the complex interaction of the two internal layers forming along the outflow boundary.

Unlike the preceding examples, the training strategy for this problem adopts a progressive four-phase schedule in which all three weights evolve simultaneously. This design is motivated by the absence of an analytical solution: the SUPG- $YZ\beta$ reference data constitutes the only available ground truth, and the weight schedule must carefully balance data fidelity with physics enforcement to avoid steering the network toward solutions that satisfy the PDE residual but deviate from the FEM reference without any means of independent verification. The data weight increases from $w_{\text{data}} = 0.1$ in Phase I to $w_{\text{data}} = 0.8$ in Phase IV, reflecting the growing importance of anchoring to the reference solution as physics enforcement intensifies. The PDE weight increases from $w_{\text{pde}} = 0.5$ to $w_{\text{pde}} = 10.0$, progressively strengthening the physics constraint. The boundary condition weight increases from $w_{\text{bc}} = 0.1$ to $w_{\text{bc}} = 1.0$, ensuring that the non-homogeneous piecewise Dirichlet data—which cannot be incorporated through a simple lift function—remains well-satisfied as the PDE loss becomes dominant. The phase boundaries and adaptive weights are reported in Table 5.

Table 5: Phase boundaries and adaptive weights used for solving *Example 5*.

| Phase | Epochs | w_{data} | w_{pde} | w_{bc} |
|-------|-----------|-------------------|------------------|-----------------|
| I | 0–999 | 0.1 | 0.5 | 0.1 |
| II | 1000–1999 | 0.35 | 0.8 | 0.3 |
| III | 2000–3499 | 0.5 | 5.0 | 0.8 |
| IV | 3500–4999 | 0.8 | 10.0 | 1.0 |

Figure 16 displays the three-dimensional solution profiles at the terminal time $t_f = 0.25$ for *Example 5*. Since no analytical solution is available for this problem, the assessment relies on qualitative comparison among the three numerical approximations. The SUPG solution (Figure 16a) captures the overall L-shaped block structure and its diagonal advection toward the upper-right corner; however, pronounced oscillatory artifacts are visible along the leading edges of the front, particularly near the corner where the horizontal and vertical arms of the L-shape meet. These crosswind oscillations, a characteristic deficiency of streamline-based stabilization in the presence of sharp transverse gradients, contaminate the flat plateau region where the solution should remain identically unity, as well as the surrounding zero-valued exterior. The addition of $YZ\beta$ shock-capturing (Figure 16b) substantially suppresses these oscillatory features, yielding a smoother and more monotone profile. The front edges are better resolved, the plateau region is flatter, and the spurious oscillations in the exterior

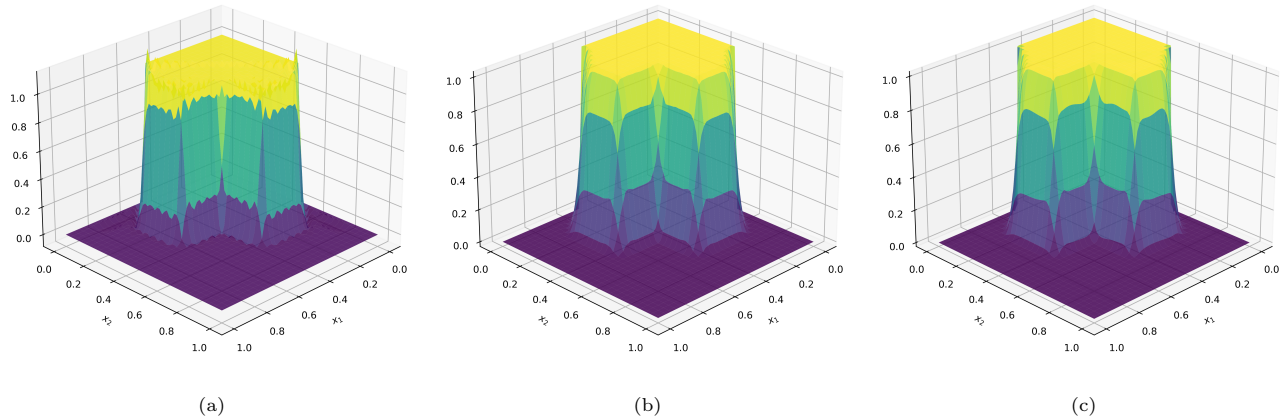


Figure 16: Three-dimensional surface plots of the solution to *Example 5* at $t_f = 0.25$ with $\varepsilon = 10^{-8}$: (a) SUPG finite element approximation; (b) SUPG- $YZ\beta$ finite element approximation; (c) hybrid PINN.

are largely eliminated. However, a slight smearing of the sharp transitions is discernible, consistent with the isotropic artificial diffusion introduced by the shock-capturing operator. The hybrid PINN correction (Figure 16c) produces a surface profile that closely resembles the SUPG- $YZ\beta$ approximation in its overall structure while exhibiting two notable improvements: the solution remains within the physically admissible range $[0, 1]$ without exhibiting the overshoot or undershoot artifacts present in the FEM approximations, and the front transitions appear marginally sharper along the leading edges of the advected L-shaped block. This improved boundedness is attributable to the combined effect of data-driven training from the well-behaved SUPG- $YZ\beta$ reference and the PDE residual regularization, which together steer the network away from nonphysical extrema.

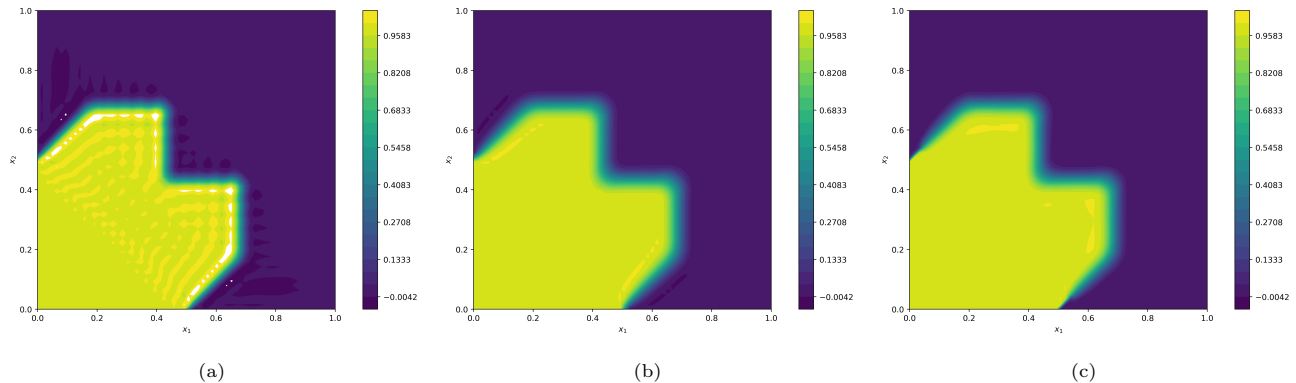


Figure 17: Contour plots of the solution to *Example 5* at $t_f = 0.25$ with $\varepsilon = 10^{-8}$: (a) SUPG finite element approximation; (b) SUPG- $YZ\beta$ finite element approximation; (c) hybrid PINN.

The contour plots in Figure 17 provide a top-down view that more clearly exposes the spatial structure of the advected L-shaped front and the differences among the three numerical approximations. The SUPG solution (Figure 17a) reveals pronounced crosswind oscillations manifesting as a series of concentric ripple-like contour distortions along the leading edges of the front. These artifacts, which extend well into both the plateau region and the zero-valued exterior, are a hallmark of insufficient crosswind diffusion for convection-dominated

transport of discontinuous initial data on structured meshes. The oscillatory pattern is particularly severe near the re-entrant corner of the L-shape, where the interaction of the horizontal and vertical fronts produces competing gradient directions that the streamline-based SUPG stabilization cannot adequately resolve. The SUPG- $YZ\beta$ solution (Figure 17b) eliminates these oscillatory features entirely, producing a smooth contour field with well-defined front boundaries. However, the front transitions are noticeably broadened compared to the initial sharp discontinuity, reflecting the isotropic artificial diffusion introduced by the shock-capturing operator. The plateau region behind the front maintains a nearly uniform value close to unity, confirming the effectiveness of the $YZ\beta$ mechanism in preserving the solution structure away from steep gradients. The hybrid PINN contour (Figure 17c) closely reproduces the SUPG- $YZ\beta$ pattern while exhibiting subtle differences along the front edges: the transition zone appears marginally narrower, suggesting that the PDE residual enforcement partially counteracts the numerical diffusion introduced by the shock-capturing operator. Furthermore, the hybrid PINN solution remains within $[0, 1]$ throughout the domain, avoiding the minor undershoot of -0.0042 visible in the colorbar of the FEM approximations—a consequence of the data fidelity and PDE residual losses jointly penalizing nonphysical solution values during training.

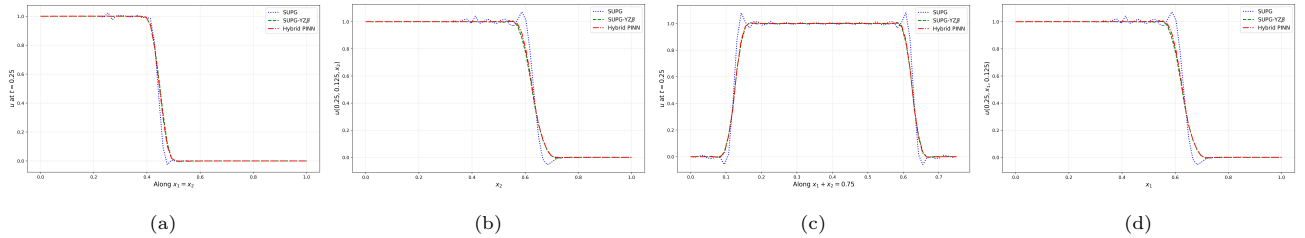


Figure 18: Cross-sectional profiles for *Example 5* at $t_f = 0.25$ with $\varepsilon = 10^{-8}$, comparing SUPG, SUPG- $YZ\beta$, and hybrid PINN: (a) along the diagonal $x_1 = x_2$; (b) along $x_1 = 0.125$ (through the vertical arm); (c) along $x_1 + x_2 = 0.75$ (perpendicular to the advection direction); (d) along $x_2 = 0.125$ (through the horizontal arm).

Figure 18 presents one-dimensional cross-sectional profiles extracted along four representative lines at the terminal time $t_f = 0.25$, providing a quantitative comparison among the three methods. The diagonal slice along $x_1 = x_2$ (Figure 18a) intersects the advected L-shaped front along the convection direction $\mathbf{b} = (\sqrt{2}/2, \sqrt{2}/2)^\top$. All three methods capture the transition from $u \approx 1$ to $u \approx 0$ near $s \approx 0.45$; however, the SUPG solution exhibits visible oscillatory overshoots in the vicinity of the front, while the SUPG- $YZ\beta$ and hybrid PINN profiles are nearly monotone. The PINN profile tracks the SUPG- $YZ\beta$ solution closely, with a marginally sharper transition at the leading edge. The vertical slice at $x_1 = 0.125$ (Figure 18b) cuts through the vertical arm of the L-shape. The plateau at $u \approx 1$ extends to $x_2 \approx 0.6$, consistent with the advection of the initial block from $x_2 \in [0, 0.5]$. The SUPG solution displays pronounced undershoots below zero near the trailing edge of the front, while both the SUPG- $YZ\beta$ and hybrid PINN solutions maintain non-negative profiles. The hybrid PINN achieves a slightly steeper descent at the front compared to the SUPG- $YZ\beta$ approximation. The slice along $x_1 + x_2 = 0.75$ (Figure 18c), oriented perpendicular to the advection direction, provides the most revealing comparison. This cross-section intersects the front transversely, where crosswind effects are most pronounced. The SUPG solution shows significant oscillatory artifacts along the entire profile, reflecting the well-known crosswind

diffusion deficiency. The SUPG- $YZ\beta$ profile is substantially smoother, though slightly broadened. The hybrid PINN follows the SUPG- $YZ\beta$ profile while maintaining boundedness within $[0, 1]$, consistent with the regularizing effect of the physics-informed training. The horizontal slice at $x_2 = 0.125$ (Figure 18d) passes through the horizontal arm of the L-shape. The front near $x_1 \approx 0.65$ shows similar behavior: the SUPG solution oscillates, the SUPG- $YZ\beta$ solution provides a smooth but diffused transition, and the hybrid PINN closely tracks the stabilized FEM reference. Across all four cross-sections, the PINN correction consistently preserves the overall solution structure of the SUPG- $YZ\beta$ approximation while empirically satisfying the maximum principle—a property that neither FEM formulation guarantees by construction. This behavior, while not enforced architecturally, arises naturally from the combination of training on bounded reference data and PDE residual minimization in the interior.

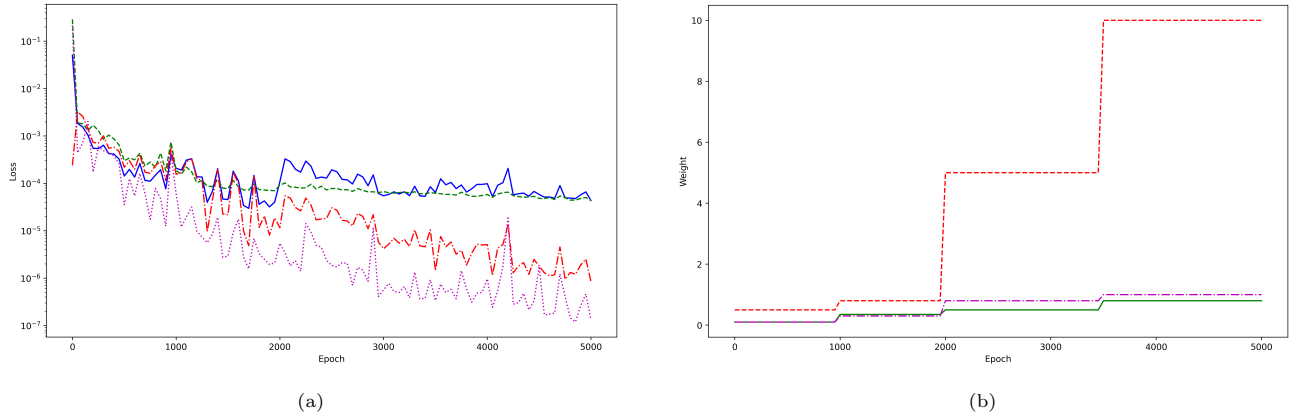


Figure 19: Training diagnostics for *Example 5* with $\varepsilon = 10^{-8}$: (a) evolution of the individual loss components (total, data, PDE, and BC) over 5000 training epochs on a logarithmic scale; (b) adaptive weight schedule w_{data} , w_{pde} , and w_{bc} governing the four-phase training strategy.

The training diagnostics for Example 5 are presented in Figure 19. The loss evolution in Figure 19a reveals the distinct behavior of each component across the four training phases. During Phase I (epochs 0–999), where the PDE weight is moderate at $w_{\text{pde}} = 0.5$ and the data weight is low at $w_{\text{data}} = 0.1$, all loss components decrease rapidly from $\mathcal{O}(10^{-1})$ to $\mathcal{O}(10^{-4})$, indicating that the network successfully learns the global solution structure from the SUPG- $YZ\beta$ reference snapshots while simultaneously beginning to satisfy the PDE constraint. The data loss stabilizes near $\mathcal{O}(10^{-4})$ by the end of Phase I and continues to decrease gradually throughout the remaining phases, confirming that the progressively increasing data weight ($w_{\text{data}} : 0.1 \rightarrow 0.8$) effectively anchors the network to the reference solution. The PDE loss exhibits intermittent spikes spanning approximately two orders of magnitude, from $\mathcal{O}(10^{-6})$ to $\mathcal{O}(10^{-4})$, persisting throughout training. These bursts arise when randomly sampled collocation points intersect the sharp L-shaped front, where the solution gradients are steep and the PDE residual magnitudes increase accordingly. Despite this volatile behavior, the PDE loss trend decreases steadily over the course of training. The BC loss remains consistently low at $\mathcal{O}(10^{-5})$ – $\mathcal{O}(10^{-7})$ throughout all phases, reflecting the effectiveness of the explicit boundary condition enforcement for the piecewise-discontinuous Dirichlet data. The weight schedule in Figure 19b illustrates the four-phase strategy adopted for this problem. The PDE weight

undergoes the most dramatic evolution, increasing from $w_{\text{pde}} = 0.5$ in Phase I through $w_{\text{pde}} = 0.8$ in Phase II to $w_{\text{pde}} = 5.0$ in Phase III, culminating at $w_{\text{pde}} = 10.0$ in Phase IV (epochs 3500–4999). This aggressive final PDE weight is necessary to drive the physics-informed refinement beyond mere data interpolation. Concurrently, the data weight increases from $w_{\text{data}} = 0.1$ to $w_{\text{data}} = 0.8$, ensuring that the network remains anchored to the SUPG-YZ β reference as the PDE constraint intensifies—a design choice motivated by the absence of an analytical solution for independent verification. The boundary condition weight increases gradually from $w_{\text{bc}} = 0.1$ to $w_{\text{bc}} = 1.0$, reflecting the growing importance of maintaining boundary fidelity for the non-homogeneous piecewise Dirichlet data as the training transitions toward physics-dominant refinement.

6. Conclusion and Future Work

This work presented a hybrid computational framework that couples stabilized finite element methods with physics-informed neural networks for the numerical solution of transient convection-dominated CDR-type partial differential equations. The methodology employs the SUPG formulation augmented with the YZ β shock-capturing operator to generate high-fidelity reference solutions, which subsequently serve as training data for a deep neural network equipped with residual blocks and random Fourier feature embeddings. Rather than training over the entire spatiotemporal domain, the PINN correction targets the last K_s temporal snapshots near the terminal time, where the network assimilates finite element data while simultaneously enforcing the governing PDE in strong form through automatic differentiation.

A central ingredient of the proposed approach is the selective physics enforcement strategy, which restricts the PDE residual loss to interior collocation points satisfying a distance-based exclusion criterion. This design choice prevents the physics-informed training from interfering with sharp boundary and internal layer structures that are already well-resolved by the stabilized finite element discretization. The multiphase adaptive weight evolution—progressing from data-dominant through transitional to physics-dominant training—proved essential for balancing data fidelity with physical consistency and for avoiding early training instabilities that typically arise when physics terms dominate before a reasonable solution approximation has been established.

The framework was validated on five benchmark problems spanning one- and two-dimensional settings: a linear parabolic equation with a boundary layer (*Example 1*), a time-dependent CDR equation with a hump changing its height (*Example 2*), a traveling internal layer problem (*Example 3*), the viscous Burgers’ equation with a moving shock front (*Example 4*), and an advection–diffusion equation with a discontinuous L-shaped interior layer (*Example 5*). Across all test cases, the hybrid PINN correction consistently improved upon the standalone SUPG-YZ β finite element solution, particularly in regions exhibiting steep gradients, moving fronts, and localized oscillatory artifacts. The results demonstrate that the proposed methodology inherits the robustness and stability of classical stabilized formulations while leveraging the representational flexibility of neural networks to achieve enhanced solution quality.

Several directions for future research emerge naturally from this study. First, the extension to three-dimensional problems represents a critical step toward practical engineering applications, including computational fluid dynamics and heat transfer in complex geometries. While the network architecture and training strategy

are dimension-agnostic by construction—the spatiotemporal input $\mathbf{z} = (t, \mathbf{x}) \in \mathbb{R}^{n_{\text{sd}}+1}$ and the Fourier feature embedding accommodate arbitrary spatial dimension—the computational cost of generating three-dimensional SUPG- $\text{YZ}\beta$ reference data and the increased collocation requirements for PDE residual evaluation introduce additional challenges that warrant systematic investigation.

Second, the application to coupled systems of PDEs, such as the incompressible Navier–Stokes equations, magnetohydrodynamic flows, and multi-species reactive transport, constitutes a compelling extension. In such settings, inter-equation coupling introduces additional nonlinearities, and the stabilization and shock-capturing parameters must account for the distinct characteristic scales of each governing equation. The diagonal scaling matrix \mathbf{Y} and residual vector \mathbf{Z} discussed in Remarks 5 and 6 provide a natural starting point for generalizing the $\text{YZ}\beta$ mechanism to vector-valued problems, while the PINN component can be extended to multi-output architectures that simultaneously approximate all solution fields.

Third, the adoption of space–time finite element formulations (see, for example, [80–84]) represents a natural and methodologically significant extension. In the current framework, spatial and temporal discretizations are treated separately: the spatial domain is discretized with stabilized finite elements while time integration is performed via the backward Euler scheme. Space–time formulations, by contrast, treat the temporal dimension on an equal footing with the spatial coordinates, constructing finite element meshes over the full spatiotemporal domain $\mathcal{Q} = (t_0, t_f] \times \Omega$ and solving the resulting variational problem in a unified manner. This approach offers several potential advantages for the proposed hybrid framework: (i) it enables local refinement simultaneously in space and time, which is particularly beneficial for problems with moving fronts and transient layer structures; (ii) SUPG stabilization and $\text{YZ}\beta$ shock-capturing extend naturally to the space–time setting, since the stabilization parameter τ_{SUPG} already incorporates both spatial and temporal scales through Eq. (9); and (iii) the PINN component, which already operates on spatiotemporal input coordinates $\mathbf{z} = (t, \mathbf{x})$ and computes temporal derivatives via automatic differentiation, is inherently compatible with a space–time discretization without architectural modification. Investigating how space–time SUPG- $\text{YZ}\beta$ reference solutions interact with the selective physics enforcement strategy—particularly whether the distance-based exclusion criterion should be generalized to a spatiotemporal metric—constitutes an important open question.

Fourth, and perhaps most significantly, the data-driven optimization of stabilization and shock-capturing parameters through PINNs offers a promising avenue for eliminating the empirical calibration that currently underpins the selection of τ_{SUPG} and ν_{SC} . Rather than relying on analytical expressions, one could train auxiliary neural networks to predict element-wise optimal stabilization parameters by minimizing a loss functional that penalizes both PDE residuals and solution oscillations. Such an approach would shift the parameter selection from heuristic formulas to a learning-based paradigm, potentially yielding superior performance across a broader class of problems without manual intervention.

Additional avenues include the incorporation of adaptive mesh refinement strategies guided by PINN-based error indicators, the exploration of more principled dynamic loss weighting mechanisms such as gradient-norm balancing or uncertainty-based scaling to replace the current empirically tuned multiphase schedule, and the investigation of transfer learning techniques that leverage trained models from one problem configuration to

accelerate convergence for related scenarios with different parameter values or geometries.

Author declarations

CRedit authorship contribution statement

SC: Conceptualization; Formal analysis; Funding acquisition; Investigation; Methodology; Software; Validation; Visualization; Writing - original draft; Writing - review & editing. **ÖU:** Conceptualization; Formal analysis; Investigation; Writing - review & editing. **SN:** Conceptualization; Formal analysis; Investigation; Writing - review & editing.

Conflict of interest

The authors have no conflicts to disclose.

Acknowledgment

The first author of this study was supported by the Scientific and Technological Research Council of Türkiye (TUBITAK) under Grant Number 225M468. The authors thank TUBITAK for its support.

References

- [1] T. J. R. Hughes, A. N. Brooks, A multi-dimensional upwind scheme with no crosswind diffusion, in: T. J. R. Hughes (Ed.), *Finite Element Methods for Convection Dominated Flows*, AMD-Vol.34, ASME, New York, 1979, pp. 19–35.
- [2] A. N. Brooks, T. J. R. Hughes, Streamline upwind/Petrov-Galerkin formulations for convection dominated flows with particular emphasis on the incompressible Navier-Stokes equations, *Computer Methods in Applied Mechanics and Engineering* 32 (1982) 199–259. doi:10.1016/0045-7825(82)90071-8.
- [3] T. E. Tezduyar, T. J. R. Hughes, Development of Time-Accurate Finite Element Techniques for First-Order Hyperbolic Systems with Particular Emphasis on the Compressible Euler Equations, NASA Technical Report NASA-CR-204772, NASA, 1982.
- [4] T. E. Tezduyar, T. J. R. Hughes, Finite element formulations for convection dominated flows with particular emphasis on the compressible Euler equations, in: *Proceedings of AIAA 21st Aerospace Sciences Meeting*, AIAA Paper 83-0125, Reno, Nevada, 1983. doi:10.2514/6.1983-125.
- [5] T. J. R. Hughes, T. E. Tezduyar, Finite element methods for first-order hyperbolic systems with particular emphasis on the compressible Euler equations, *Computer Methods in Applied Mechanics and Engineering* 45 (1984) 217–284. doi:10.1016/0045-7825(84)90157-9.
- [6] T. J. R. Hughes, L. P. Franca, G. M. Hulbert, A new finite element formulation for computational fluid dynamics: VIII. The Galerkin/least-squares method for advective-diffusive equations, *Computer Methods in Applied Mechanics and Engineering* 73 (1989) 173–189. doi:10.1016/0045-7825(89)90111-4.
- [7] T. J. R. Hughes, Multiscale phenomena: Green’s functions, the Dirichlet-to-Neumann formulation, subgrid scale models, bubbles and the origins of stabilized methods, *Computer Methods in Applied Mechanics and Engineering* 127 (1995) 387–401. doi:10.1016/0045-7825(95)00844-9.
- [8] T. E. Tezduyar, S. Mittal, R. Shih, Time-accurate incompressible flow computations with quadrilateral velocity-pressure elements, *Computer Methods in Applied Mechanics and Engineering* 87 (1991) 363–384. doi:10.1016/0045-7825(91)90014-W.

- [9] L. P. Franca, S. L. Frey, T. J. R. Hughes, Stabilized finite element methods: I. Application to the advective-diffusive model, *Computer Methods in Applied Mechanics and Engineering* 95 (1992) 253–276. doi:10.1016/0045-7825(92)90143-8.
- [10] T. E. Tezduyar, Y. Osawa, Finite element stabilization parameters computed from element matrices and vectors, *Computer Methods in Applied Mechanics and Engineering* 190 (2000) 411–430. doi:10.1016/S0045-7825(00)00211-5.
- [11] L. P. Franca, F. Valentin, On an improved unusual stabilized finite element method for the advective–reactive–diffusive equation, *Computer Methods in Applied Mechanics and Engineering* 190 (2000) 1785–1800. doi:10.1016/S0045-7825(00)00190-0.
- [12] T. J. R. Hughes, G. Scovazzi, L. P. Franca, Multiscale and stabilized methods, in: E. Stein, R. de Borst, T. J. R. Hughes (Eds.), *Encyclopedia of Computational Mechanics*, 2004. doi:10.1002/9781119176817.ecm2051.
- [13] E. Burman, P. Hansbo, Edge stabilization for Galerkin approximations of convection–diffusion–reaction problems, *Computer Methods in Applied Mechanics and Engineering* 193 (2004) 1437–1453. doi:10.1016/j.cma.2003.12.032.
- [14] V. John, P. Knobloch, On spurious oscillations at layers diminishing (SOLD) methods for convection-diffusion equations: Part I–A review, *Computer Methods in Applied Mechanics and Engineering* 196 (2007) 2197–2215. doi:10.1016/j.cma.2006.11.013.
- [15] L. P. Franca, G. Hauke, A. Masud, Revisiting stabilized finite element methods for the advective–diffusive equation, *Computer Methods in Applied Mechanics and Engineering* 195 (2006) 1560–1572. doi:10.1016/j.cma.2005.05.028.
- [16] V. John, P. Knobloch, On spurious oscillations at layers diminishing (SOLD) methods for convection-diffusion equations: Part II–Analysis for P_1 and Q_1 finite elements, *Computer Methods in Applied Mechanics and Engineering* 197 (2008) 1997–2014. doi:10.1016/j.cma.2007.12.019.
- [17] V. John, E. Schmeier, Finite element methods for time-dependent convection–diffusion–reaction equations with small diffusion, *Computer Methods in Applied Mechanics and Engineering* 198 (2008) 475–494. doi:10.1016/j.cma.2008.08.016.
- [18] R. Codina, Analysis of a stabilized finite element approximation of the Oseen equations using orthogonal subscales, *Applied Numerical Mathematics* 58 (2008) 264–283. doi:10.1016/j.apnum.2006.11.011.
- [19] C. Jiang, Z. Zhang, X. Han, G. Liu, G. Gao, T. Lin, A quasi-implicit characteristic–based penalty finite-element method for incompressible laminar viscous flows, *International Journal for Numerical Methods in Engineering* 114 (2018) 147–171. doi:10.1002/nme.5738.
- [20] M. Liu, G. Gao, H. Zhu, C. Jiang, A cell-based smoothed finite element method stabilized by implicit SUPG/SPGP/Fractional step method for incompressible flow, *Engineering Analysis with Boundary Elements* 124 (2021) 194–210. doi:10.1016/j.enganabound.2020.12.018.
- [21] C. Jiang, C. Hong, T. Wang, G. Zhou, N-side cell-based smoothed finite element method for incompressible flow with heat transfer problems, *Engineering Analysis with Boundary Elements* 146 (2023) 749–766. doi:10.1016/j.enganabound.2022.11.025.
- [22] M. Liu, C. Jiang, B. C. Khoo, H. Zhu, G. Gao, A cell-based smoothed finite element model for the analysis of turbulent flow using realizable k - ϵ model and mixed meshes, *Journal of Computational Physics* 501 (2024) 112783. doi:10.1016/j.jcp.2024.112783.
- [23] S. Cengizci, H. F. Öztöp, S. Natesan, A discontinuity-capturing SUPG finite element framework for simulating haptotaxis-driven cancer invasion, *Mathematics and Computers in Simulation* 241 (2026) 271–292. doi:10.1016/j.matcom.2025.10.011.
- [24] D. Ray, J. S. Hesthaven, An artificial neural network as a troubled-cell indicator, *Journal of Computational Physics* 367 (2018) 166–191. doi:10.1016/j.jcp.2018.04.029.
- [25] D. Ray, J. S. Hesthaven, Detecting troubled-cells on two-dimensional unstructured grids using a neural network, *Journal of Computational Physics* 397 (2019) 108845. doi:10.1016/j.jcp.2019.07.043.

- [26] M. H. Veiga, R. Abgrall, Towards a general stabilisation method for conservation laws using a multilayer perceptron neural network: 1D scalar and system of equations, in: European Conference on Computational Mechanics and VII European Conference on Computational Fluid Dynamics (ECCM-ECFD 2018), Glasgow, UK, 2018, pp. 2525–2550. 11–15 June 2018.
- [27] N. Discacciati, J. S. Hesthaven, D. Ray, Controlling oscillations in high-order discontinuous Galerkin schemes using artificial viscosity tuned by neural networks, *Journal of Computational Physics* 409 (2020) 109304. doi:10.1016/j.jcp.2020.109304.
- [28] L. Schwander, D. Ray, J. S. Hesthaven, Controlling oscillations in spectral methods by local artificial viscosity governed by neural networks, *Journal of Computational Physics* 431 (2021) 110144. doi:10.1016/j.jcp.2021.110144.
- [29] M. Raissi, P. Perdikaris, G. E. Karniadakis, Physics-informed neural networks: A deep learning framework for solving forward and inverse problems involving nonlinear partial differential equations, *Journal of Computational Physics* 378 (2019) 686–707. doi:10.1016/j.jcp.2018.10.045.
- [30] G. E. Karniadakis, I. G. Kevrekidis, L. Lu, P. Perdikaris, S. Wang, L. Yang, Physics-informed machine learning, *Nature Reviews Physics* 3 (2021) 422–440. doi:10.1038/s42254-021-00314-5.
- [31] S. K. Mitusch, S. W. Funke, M. Kuchta, Hybrid FEM-NN models: Combining artificial neural networks with the finite element method, *Journal of Computational Physics* 446 (2021) 110651. doi:10.1016/j.jcp.2021.110651.
- [32] A. Logg, K.-A. Mardal, G. Wells, Automated solution of differential equations by the finite element method: The FEniCS book, volume 84 of *Lecture Notes in Computational Science and Engineering*, Springer-Verlag Berlin Heidelberg, 2012. doi:10.1007/978-3-642-23099-8.
- [33] M. Alnæs, J. Blechta, J. Hake, A. Johansson, B. Kehlet, A. Logg, C. Richardson, J. Ring, M. E. Rognes, G. N. Wells, The FEniCS project version 1.5, *Archive of Numerical Software* 3 (2015) 9–23. doi:10.11588/ans.2015.100.20553.
- [34] S. Mitusch, S. W. Funke, J. S. Dokken, dolfin-adjoint 2018.1: automated adjoints for FEniCS and Firedrake, *Journal of Open Source Software* 4 (2019) 1292. doi:10.21105/joss.01292.
- [35] S. Huang, W. Feng, C. Tang, Z. He, C. Yu, J. Lv, Partial differential equations meet deep neural networks: A survey, *IEEE Transactions on Neural Networks and Learning Systems* 36 (2025) 13649–13669. doi:10.1109/tnnls.2025.3545967.
- [36] X. Jin, S. Cai, H. Li, G. E. Karniadakis, NSFnets (Navier-Stokes flow nets): Physics-informed neural networks for the incompressible Navier-Stokes equations, *Journal of Computational Physics* 426 (2021) 109951. doi:10.1016/j.jcp.2020.109951.
- [37] J. Yu, J. S. Hesthaven, A data-driven shock capturing approach for discontinuous Galekin methods, *Computers & Fluids* 245 (2022) 105592. doi:10.1016/j.compfluid.2022.105592.
- [38] S. Yadav, S. Ganesan, SPDE-ConvNet: Solve singularly perturbed partial differential equation with deep learning, in: 8th European Congress on Computational Methods in Applied Sciences and Engineering (ECCOMAS Congress 2022), Oslo, Norway, 2022. 5–9 June 2022.
- [39] T.-H. Huang, Stabilized and variationally consistent integrated meshfree formulation for advection-dominated problems, *Computer Methods in Applied Mechanics and Engineering* 403 (2023) 115698. doi:10.1016/j.cma.2022.115698.
- [40] T. Le-Duc, H. Nguyen-Xuan, J. Lee, A finite-element-informed neural network for parametric simulation in structural mechanics, *Finite Elements in Analysis and Design* 217 (2023) 103904. doi:10.1016/j.finel.2022.103904.
- [41] S. Yadav, S. Ganesan, Artificial neural network-augmented stabilized finite element method, *Journal of Computational Physics* 499 (2024) 112702. doi:10.1016/j.jcp.2023.112702.
- [42] R. Khodayi-Mehr, M. M. Zavlanos, VarNet: Variational neural networks for the solution of partial differential equations, 2019. doi:10.48550/arxiv.1912.07443.

- [43] K. A. Luong, T. Le-Duc, J. Lee, Automatically imposing boundary conditions for boundary value problems by unified physics-informed neural network, *Engineering with Computers* 40 (2024) 1717–1739. doi:10.1007/s00366-023-01871-2.
- [44] T. G. Grossmann, U. J. Komorowska, J. Latz, C.-B. Schönlieb, Can physics-informed neural networks beat the finite element method?, *IMA Journal of Applied Mathematics* 89 (2024) 143–174. doi:10.1093/imamat/hxae011.
- [45] Y. Yamazaki, A. Harandi, M. Muramatsu, A. Viardin, M. Apel, T. Brepols, S. Reese, S. Rezaei, A finite element-based physics-informed operator learning framework for spatiotemporal partial differential equations on arbitrary domains, *Engineering with Computers* 41 (2024) 1–29. doi:10.1007/s00366-024-02033-8.
- [46] F. Buzaev, J. Gao, I. Chuprov, E. Kazakov, Hybrid acceleration techniques for the physics-informed neural networks: a comparative analysis, *Machine Learning* 113 (2023) 3675–3692. doi:10.1007/s10994-023-06442-6.
- [47] W. Yufeng, X. Cong, Y. Min, Z. Jin, Less emphasis on hard regions: Curriculum learning of PINNs for singularly perturbed convection-diffusion-reaction problems, *East Asian Journal on Applied Mathematics* 14 (2024) 104–123. doi:10.4208/eajam.2023-062.170523.
- [48] T. Y. Chang, G. M. Gie, Y. Hong, C. Y. Jung, Singular layer PINN methods for Burgers’ equation, *arXiv preprint arXiv:2410.09723* (2024).
- [49] T.-Y. Chang, G.-M. Gie, Y. Hong, C.-Y. Jung, Singular layer physics informed neural network method for plane parallel flows, *Computers & Mathematics with Applications* 166 (2024) 91–105. doi:10.1016/j.camwa.2024.04.025.
- [50] D. Frerichs-Mihov, L. Henning, V. John, On loss functionals for physics-informed neural networks for steady-state convection-dominated convection-diffusion problems, *Communications on Applied Mathematics and Computation* (2024). doi:10.1007/s42967-024-00433-7.
- [51] T.-Y. Hsieh, T.-H. Huang, A multiscale stabilized physics informed neural networks with weakly imposed boundary conditions transfer learning method for modeling advection dominated flow, *Engineering with Computers* 40 (2024) 3353–3387. doi:10.1007/s00366-024-01981-5.
- [52] M. Kütük, H. Yücel, Energy dissipation preserving physics informed neural network for Allen–Cahn equations, *Journal of Computational Science* 87 (2025) 102577. doi:10.1016/j.jocs.2025.102577.
- [53] A. Raina, S. Badireddi, S. Natesan, Application of PINN to obtain solution of boundary layer problems arising in fluid dynamics, *Mathematical Foundations of Computing* 0 (2025) 1–20. doi:10.3934/mfc.2025024.
- [54] S. Cengizci, O. Uğur, S. Natesan, A PINN-enhanced SUPG-stabilized hybrid finite element framework with shock-capturing for computing steady convection-dominated flows, *Advances in Engineering Software* 216 (2026) 104135. doi:10.1016/j.advengsoft.2026.104135.
- [55] T. E. Tezduyar, Computation of moving boundaries and interfaces and stabilization parameters, *International Journal for Numerical Methods in Fluids* 43 (2003) 555–575. doi:10.1002/flid.505.
- [56] T. E. Tezduyar, M. Senga, Stabilization and shock-capturing parameters in SUPG formulation of compressible flows, *Computer Methods in Applied Mechanics and Engineering* 195 (2006) 1621–1632. doi:10.1016/j.cma.2005.05.032.
- [57] S. Cengizci, O. Uğur, S. Natesan, SUPG- $YZ\beta$ computation of chemically reactive convection-dominated nonlinear models, *International Journal of Computer Mathematics* 100 (2022) 283–303. doi:10.1080/00207160.2022.2114794.
- [58] S. Cengizci, O. Uğur, S. Natesan, SUPG-based stabilized finite element computations of convection-dominated 3D elliptic PDEs using shock-capturing, *Journal of Computational and Applied Mathematics* 451 (2024) 116022. doi:10.1016/j.cam.2024.116022.
- [59] F. Shakib, Finite element analysis of the compressible Euler and Navier-Stokes equations, Ph.D. thesis, Department of Mechanical Engineering, Stanford University, 1988.

- [60] T. E. Tezduyar, Stabilized finite element formulations for incompressible flow computations, *Advances in Applied Mechanics* 28 (1992) 1–44. doi:10.1016/S0065-2156(08)70153-4.
- [61] S. Cengizci, An enhanced SUPG-stabilized finite element formulation for simulating natural phenomena governed by coupled system of reaction-convection-diffusion equations, *Mathematical Modelling and Numerical Simulation with Applications* 3 (2023) 297–317. doi:10.53391/mmnsa.1387125.
- [62] S. Cengizci, O. Uğur, A stabilized FEM formulation with discontinuity-capturing for solving Burgers'-type equations at high Reynolds numbers, *Applied Mathematics and Computation* 442 (2023) 127705. doi:10.1016/j.amc.2022.127705.
- [63] S. Cengizci, O. Uğur, SUPG formulation augmented with $YZ\beta$ shock-capturing for computing shallow-water equations, *ZAMM - Journal of Applied Mathematics and Mechanics / Zeitschrift für Angewandte Mathematik und Mechanik* 103 (2023). doi:10.1002/zamm.202200232.
- [64] S. Cengizci, O. Uğur, A computational study for simulating MHD duct flows at high Hartmann numbers using a stabilized finite element formulation with shock-capturing, *Journal of Computational Science* 81 (2024) 102381. doi:10.1016/j.jocs.2024.102381.
- [65] S. Cengizci, O. Uğur, A computational study for pricing European- and American-type options under Heston's stochastic volatility model: Application of the SUPG- $YZ\beta$ formulation, *Computational Economics* (2024). doi:10.1007/s10614-024-10704-3.
- [66] T. E. Tezduyar, Finite element methods for fluid dynamics with moving boundaries and interfaces, in: E. Stein, R. D. Borst, T. J. R. Hughes (Eds.), *Encyclopedia of Computational Mechanics, Volume 3: Fluids*, Wiley, 2004. doi:10.1002/0470091355.ecm069.
- [67] T. E. Tezduyar, M. Senga, SUPG finite element computation of inviscid supersonic flows with $YZ\beta$ shock-capturing, *Computers & Fluids* 36 (2007) 147–159. doi:10.1016/j.compfluid.2005.07.009.
- [68] T. E. Tezduyar, M. Senga, D. Vicker, Computation of inviscid supersonic flows around cylinders and spheres with the SUPG formulation and $YZ\beta$ shock-capturing, *Computational Mechanics* 38 (2006) 469–481. doi:10.1007/s00466-005-0025-6.
- [69] Y. Bazilevs, V. M. Calo, T. E. Tezduyar, T. J. R. Hughes, $YZ\beta$ discontinuity capturing for advection-dominated processes with application to arterial drug delivery, *International Journal for Numerical Methods in Fluids* 54 (2007) 593–608. doi:10.1002/flid.1484.
- [70] I. Loshchilov, F. Hutter, Decoupled weight decay regularization, 2017. doi:10.48550/arXiv.1711.05101. arXiv:1711.05101.
- [71] D. P. Kingma, J. L. Ba, Adam: A method for stochastic optimization, in: *ICLR 2015: International Conference on Learning Representations*, ArXiv, Ithaca, NY, 2015, p. 13.
- [72] M. Tancik, P. P. Srinivasan, B. Mildenhall, S. Fridovich-Keil, N. Raghavan, U. Singhal, R. Ramamoorthi, J. T. Barron, R. Ng, Fourier features let networks learn high frequency functions in low dimensional domains, in: *Advances in Neural Information Processing Systems (NeurIPS 2020)*, Vancouver, Canada, 2020.
- [73] H. P. Langtangen, A. Logg, Solving PDEs in Python: The FEniCS Tutorial I, volume 3 of *Simula SpringerBriefs on Computing*, Springer International Publishing, 2016.
- [74] I. A. Baratta, J. P. Dean, J. S. Dokken, M. Habera, J. S. Hale, C. N. Richardson, M. E. Rognes, M. W. Scroggs, N. Sime, G. N. Wells, DOLFINx: The next generation FEniCS problem solving environment, 2023. doi:10.5281/zenodo.10447666.
- [75] A. Paszke, S. Gross, F. Massa, A. Lerer, J. Bradbury, G. Chanan, T. Killeen, Z. Lin, N. Gimelshein, L. Antiga, A. Desmaison, A. Kopf, E. Yang, Z. DeVito, M. Raison, A. Tejani, S. Chilamkurthy, B. Steiner, L. Fang, J. Bai, S. Chintala, PyTorch: An imperative style, high-performance deep learning library, in: *Proceedings of the 32nd Conference on Neural Information Processing Systems*, volume 32, Curran Associates, Inc., Vancouver, Canada, 2019.

- [76] S. Balay, S. Abhyankar, M. F. Adams, S. Benson, J. Brown, P. Brune, K. Buschelman, E. Constantinescu, L. Dalcin, A. Dener, V. Eijkhout, J. Faibussowitsch, W. D. Gropp, V. Hapla, T. Isaac, P. Jolivet, D. Karpeev, D. Kaushik, M. G. Knepley, F. Kong, S. Kruger, D. A. May, L. C. McInnes, R. T. Mills, L. Mitchell, T. Munson, J. E. Roman, K. Rupp, P. Sanan, J. Sarich, B. F. Smith, H. Suh, S. Zampini, H. Zhang, H. Zhang, J. Zhang, PETSc/TAO Users Manual, Technical Report ANL-21/39 - Revision 3.23, Argonne National Laboratory, 2025. doi:10.2172/2565610.
- [77] Y. Saad, M. Schultz, GMRES: A generalized minimal residual algorithm for solving nonsymmetric linear systems, *SIAM Journal of Scientific and Statistical Computing* 7 (1986) 856–869. doi:10.1137/0907058.
- [78] S. Gowrisankar, S. Natesan, Robust numerical scheme for singularly perturbed convection–diffusion parabolic initial–boundary-value problems on equidistributed grids, *Computer Physics Communications* 185 (2014) 2008–2019. doi:10.1016/j.cpc.2014.04.004.
- [79] S. Giere, T. Iliescu, V. John, D. Wells, SUPG reduced order models for convection-dominated convection–diffusion–reaction equations, *Computer Methods in Applied Mechanics and Engineering* 289 (2015) 454–474. doi:10.1016/j.cma.2015.01.020.
- [80] T. J. R. Hughes, G. M. Hulbert, Space-time finite element methods for elastodynamics: Formulations and error estimates, *Computer Methods in Applied Mechanics and Engineering* 66 (1988) 339–363. doi:10.1016/0045-7825(88)90006-0.
- [81] S. Mittal, T. E. Tezduyar, Notes on the stabilized space-time finite-element formulation of unsteady incompressible flows, *Computer Physics Communications* 73 (1992) 93–112. doi:10.1016/0010-4655(92)90031-s.
- [82] T. E. Tezduyar, S. Sathe, Modeling of fluid–structure interactions with the space–time finite elements: Solution techniques, *International Journal for Numerical Methods in Fluids* 54 (2007) 855–900. doi:10.1002/fld.1430.
- [83] T. E. Tezduyar, S. Sathe, R. Keedy, K. Stein, Space–time finite element techniques for computation of fluid–structure interactions, *Computer Methods in Applied Mechanics and Engineering* 195 (2006) 2002–2027. doi:10.1016/j.cma.2004.09.014.
- [84] O. Steinbach, Space-time finite element methods for parabolic problems, *Computational Methods in Applied Mathematics* 15 (2015) 551566. doi:10.1515/cmam-2015-0026.